*J. Fluid Mech.* (1991), *vol.* 222, *pp.* 293–327
*Printed in Great Britain*



# On the structure of high-Reynolds-number supersonic turbulent boundary layers

By ERIC F. SPINA†, JOHN F. DONOVAN‡ AND ALEXANDER J. SMITS

Princeton University Gas Dynamics Laboratory, Princeton, New Jersey, USA

(Received 10 May 1989 and in revised form 9 June 1990)

Experimental results are presented that reveal key features of the large-scale organized structures in a supersonic, turbulent boundary layer. Measurements were obtained in a Mach 3 zero-pressure-gradient boundary layer using a crossed-wire probe and arrays of normal hot wires with vertical, spanwise, and streamwise separations ranging from 0.1 to $0.6\delta$. Space–time correlation results indicate the existence of large-scale structures of a size comparable to $\delta$, with a spanwise extent only slightly less than the vertical scale. The convection velocity of the large-scale motions is nearly constant across 80% of the boundary layer and is equal to approximately $0.9U_\infty$.

It is shown that positive events detected with the VITA conditional sampling technique correspond to steep gradients in the streamwise mass flux which extend across most of the boundary layer. These sharp gradients appear to be the upstream interfaces of large-scale turbulent 'bulges', similar to those seen in incompressible boundary layers. In a reference frame moving with the convection speed of the sharp gradients, low-momentum fluid is observed rotating on a large-scale, while high-momentum fluid forms a saddle point on the upstream edge of the large-scale motion. These motions are associated with elevated levels of the shear product, emphasizing their role in the dynamics of the boundary layer.

## 1. Introduction

This paper extends the work of Spina & Smits (1987), who used space–time correlations in the wall-normal (vertical) direction to determine the existence of large-scale structures in high-Reynolds-number, supersonic boundary layers. Whereas the previous investigation primarily used normal hot wires with a limited vertical separation, the present study examines both the vertical and spanwise extent of the organized motions with significantly larger wire separations. In addition, streamwise-separated hot wires are used to determine the convection velocity, and crossed wires are used to detect two velocity components and to attribute an ensemble-averaged flow field to the large-scale structures. Using these techniques, a clearer picture of the organized structures in supersonic, turbulent boundary layers is developed.

It has been known for some time that the fluid motions in a turbulent boundary layer are not random, but are, to some extent, 'organized'. However, for many years

† Present address: Syracuse University, Mechanical and Aerospace Engineering Dept, Syracuse, NY, USA.

‡ Present address: McDonnell Douglas Research Laboratory, St Louis, MO, USA.

the motions were considered to be too complex to perform anything beyond a time-averaged analysis of the corresponding turbulent signals. This type of analysis has significant limitations which prevent a complete understanding of the important time-dependent, physical mechanisms of turbulence. It may be this lack of understanding which has prevented the accurate prediction of many complex boundary-layer flows. Over the past 30 years, however, much progress has been made in formulating a picture of the organized motions in boundary layers. It has been firmly established that incompressible turbulent boundary layers are populated with a hierarchy of quasi-deterministic organized structures which are crucial to the maintenance of the turbulent flow. The primary aim of this study is to extend these ideas to high-Reynolds-number, supersonic boundary layers.

There is now considerable evidence for the presence of organized structures in supersonic flows. For example, Head & Bandyopadhyay (1981) found support for their hairpin vortex hypothesis from the schlieren photographs of Deckker & Weekes (1976) and Deckker (1980) in supersonic boundary layers. While the photographs do not contain incontrovertible evidence of hairpin vortices, the boundary layers are shown to contain coherent density structures inclined at about 45° to the wall. In addition, James (1958) presented shadowgraphs of flow over axisymmetric bodies of revolution in a Mach 3.1 flow, and the coarse, granular structure of the boundary layer indicates the presence of large-scale, downstream-leaning flow structures similar to those seen in incompressible flows. Seiff & Short (1958) observed similar features at $M = 3.5$.

Zakkay, Barra & Wang (1979) took measurements with a five hot-wire rake in a high-Reynolds-number, subsonic, compressible boundary layer ($Re_\theta = 108000$, $M_\infty = 0.64$). They found appreciable correlations over the range of vertical spacings investigated, but the maximum spacing was limited to $0.125\delta$. Owen & Horstman (1972) made extensive space–time correlation measurements in a hypersonic boundary layer ($Re_\theta = 5800$–$12000$, $M_\infty = 7.2$). They focused on mean convection velocities, which were found to be approximately $0.8U_\infty$ in the outer part of the boundary layer. They also traversed a hot wire vertically across the boundary layer, directly above another wire located at $y/\delta = 0.06$, and found evidence of large-scale motions spanning the entire boundary layer, inclined to the wall at angles ranging from 20° to 60°.

More recently, Robinson (1986*a*) performed a dual hot-wire survey in a supersonic boundary layer ($Re_\theta = 15000$, $M_\infty = 2.97$). Robinson fixed one wire at $y/\delta = 0.02$ ($y^+ = 29$) and traversed the second wire directly above. The significant level of correlation which Robinson measured suggests the existence of an average large-scale motion which spans the entire boundary layer. Similar to observations in incompressible flows, Robinson detected structures with an average angle of 5° near the wall and 30° at $y/\delta = 0.6$. Spina & Smits (1987) traversed two hot wires with a fixed vertical separation of $0.1\delta$ across the boundary layer in a Mach 2.9 flow ($Re_\theta = 81000$). The resulting cross-correlations indicate that the large-scale structures extend across the majority of the boundary layer, and are inclined at an average angle of 45°. Conditional sampling was used to examine the individual structure angles, which were found to have a standard deviation of 20°. They used wall-pressure/mass-flux correlations to determine the spanwise extent of the large-scale motions, which was less than $0.3\delta$.

Smith & Smits (1988) performed flow visualization in the same boundary layer used for this study. They used a high-framing-rate camera in conjunction with the traditional schlieren technique in an attempt to track the large-scale structures as

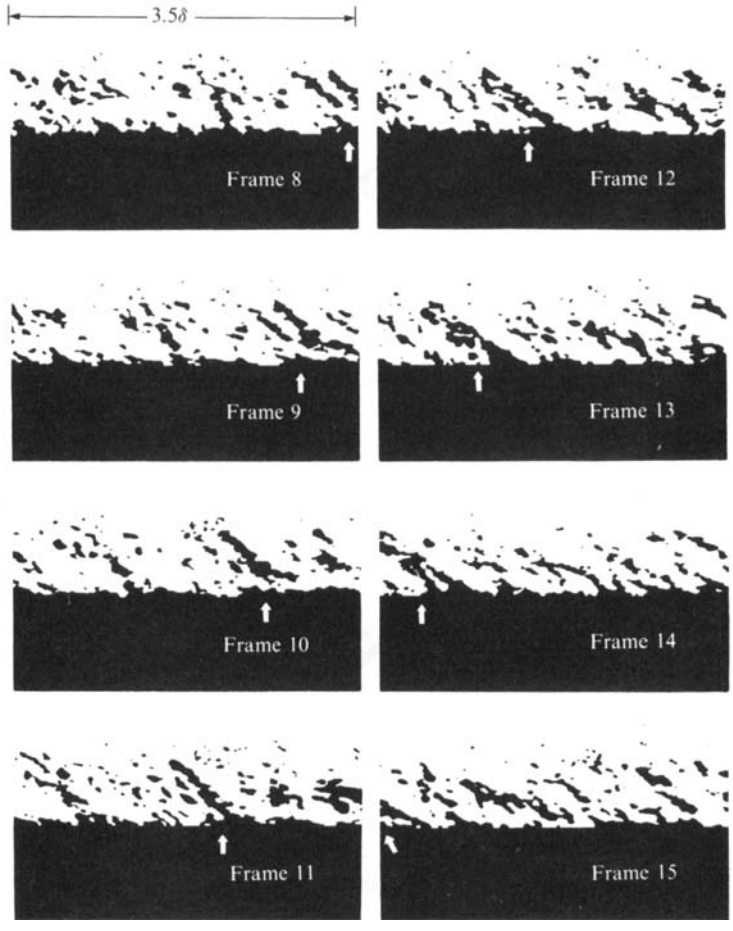


FIGURE 1. Time sequence of image-processed positive-density-gradient structures in a supersonic boundary layer; Smith & Smits (1988). The flow is from right to left and the time interval between frames is 27 μs ($TU_\infty/\delta \approx 0.54$). The arrow follows a single large-scale structure as it convects downstream.

they evolved in the boundary layer. The schlieren method relies upon density gradient variations to provide a non-intrusive method for viewing large-scale motions in a supersonic boundary layer. Schlieren has the disadvantage of integrating along the entire optical path ($8\delta$ in this case), but the sharp, energetic, large-scale structures which were visualized (figure 1) provide evidence for the existence of organized motions.

Smith & Smits were able to detect two different types of motions: 'positive' structures which have a strong positive density gradient in the upstream direction, and 'negative' structures which have a strong negative density gradient in the upstream direction. Significant differences were observed between positive and negative structures. First, the positive structures were well-defined, with a typical inclination angle of 30–50° to the wall; while the negative structures seemed less coherent, and were inclined at approximately 70°. More significantly, to detect approximately the same number of positive and negative structures, it was necessary to set the effective threshold much lower to detect negative structures, indicating that they are weaker. Since density and streamwise velocity fluctuations are strongly

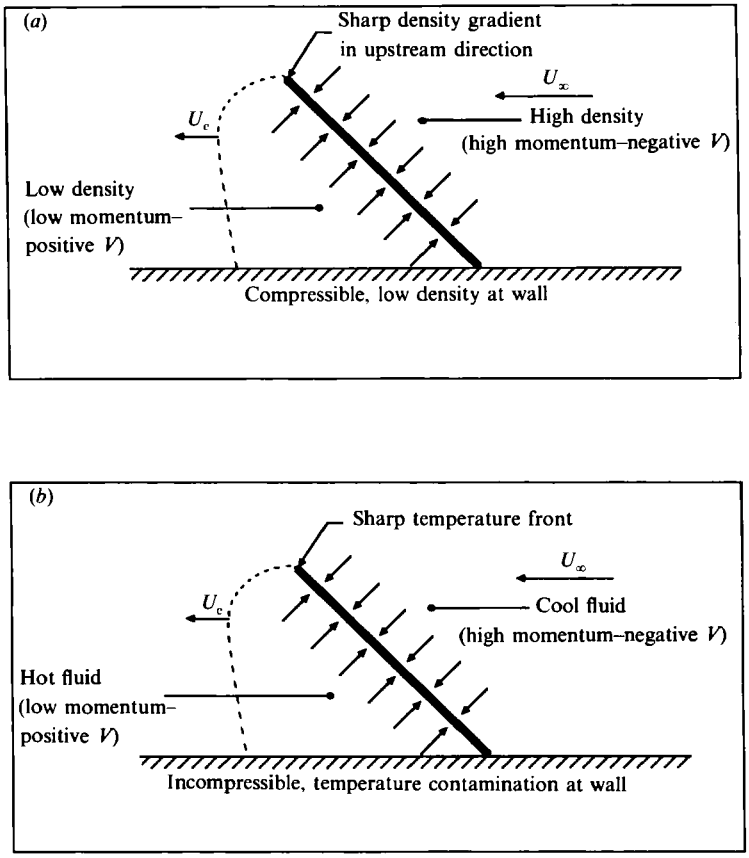


FIGURE 2. Qualitative comparison between the detected structures of: (*a*) Smith & Smits (1988) in a supersonic boundary layer (visual detection), and (*b*) Chen & Blackwelder (1978) in a subsonic boundary layer over a heated wall (probe detection).

correlated (see, for example, Dussauge & Gaviglio 1981), the strong positive density structure may be interpreted as a sharp increase in fluctuating streamwise velocity on the upstream edge of a large-scale 'finger' or 'bulge', as was observed in incompressible flows (Kovasznay, Kibens & Blackwelder 1970; Brown & Thomas 1977; Falco 1977). Consecutive image-processed frames illustrating positive structures are reproduced from Smith & Smits in figure 1, and a schematic illustrating a possible interpretation is presented in figure 2(*a*). This interpretation is consistent with the heated-wall studies performed by Chen & Blackwelder (1978) and Cheng & Ng (1982) in low-speed flows. These researchers found similar structures in incompressible boundary layers, but the low-density 'fronts' were replaced by high-temperature fronts (see figure 2*b*). Smith & Smits measured the convection velocity of individual density structures from the high-speed movie, and the distribution was found to be centred about $0.9U_\infty$. Furthermore, the convection velocity of the individual structures was determined to be approximately constant across the middle 60% of the boundary layer.

It is evident that the qualitative features of the outer-layer structure of turbulent boundary layers, which are extensively documented in incompressible flows, do indeed extend to high-Reynolds-number, supersonic flows. However, the measurements in compressible flows have been primarily concerned with the detection of

| | |
|---|---|
| $M_\infty$ | 2.87 |
| $Re_\theta$ | 81000 |
| $\delta^+$ | 10000 |
| $\delta$ | 28 mm |
| $\delta^*$ | 6.2 mm |
| $\theta$ | 1.2 mm |
| $U_\infty$ | 565 m/s |
| $(\overline{\rho u})_\infty$ | 479 kg/m$^2$ s |
| $P_{\text{wall}}$ | $2.3 \times 10^4$ N/m$^2$ (3.34 p.s.i) |
| $C_f$ | 0.001 14 |

TABLE 1. Flow conditions on the centreline at the measurement location

the large-scale motions, and not the definition of their kinematics and internal structure. The present study aims to provide the first detailed measurements of this kind.

It is important to emphasize at the outset that the data gathered in this experiment are from the outer region of the boundary layer. Owing to the high Reynolds number of the flow, the nearest measurement station to the wall is $1000y^+$ ($y/\delta \approx 0.1$), and the results to be presented are therefore not directly related to near-wall bursting activity.

## 2. The experiment

The flow investigated was a naturally-turbulent, zero-pressure-gradient boundary layer at Mach 2.9 and $Re_\theta = 81000$, which developed on the wind-tunnel floor. In preliminary work, a complete set of mean-flow measurements was taken to characterize the boundary layer. The results (discussed in Spina & Smits 1987) indicate that the flow is typical of a high-Reynolds-number, well-developed turbulent boundary layer, with negligible three-dimensionality. (Complete documentation of the mean flow is provided in Smits & Dussauge 1989, case CAT8603T.) The flow conditions at the measurement station are provided in table 1.

Constant-temperature hot-wire anemometry was used to measure turbulent fluctuations at several locations simultaneously. When multiple probes were used, great care was taken in their positioning so that a separation between the wires occurred only in the stated direction. All hot-wire combinations were checked for local blockage using optical techniques as well as by monitoring the r.m.s. of the signal. Furthermore, the frequency response of the wires was matched as closely as possible, so that relative phase shift was minimized. Both normal-wire and crossed-wire probes were used, and their construction, calibration, and use in supersonic flow is documented in Smits, Hayakawa & Muck (1983) and Donovan & Spina (1990). It is important to point out that a normal hot wire used in supersonic flow yields the streamwise fluctuating mass flux, $(\rho u)'$, and not simply the streamwise fluctuating velocity, $u'$. (In this paper the primed quantities denote fluctuations from the mean.) The relation between $(\rho u)'$ and $u'$ is not a trivial one; both density and velocity fluctuations contribute to the mass-flux fluctuations. This issue is addressed in Appendix A.

The data acquisition system is fully described in Spina & Smits (1987). Up to four signals were sampled simultaneously at 1 MHz per channel, with a continuous record length of 32K data points per channel.

## 3. Two-point correlation results and discussion

In this section, results are presented from hot-wire measurements obtained simultaneously at two separate locations within the boundary layer. The transducer separations were varied from $0.1\delta$ to $0.6\delta$ over vertical, spanwise, and streamwise distances, with the intent of extracting information about the large-scale structures in the boundary layer.

The analysis tool utilized in this section, space–time correlations, provides average information about the turbulent scales in the flow. Although the eventual goal is to describe the boundary layer on an instantaneous basis, the results presented here reveal the dominant scales, and allow comparison of this work to previous low-speed, low-Reynolds-number results.

### 3.1. *Streamwise hot-wire separations*

To measure the convection velocity of the organized structures, two normal hot wires with fixed streamwise separations of $\xi_1 = 0.11\delta$, $0.16\delta$ and $0.18\delta$ were traversed vertically across the boundary layer. Whenever two probes are placed one behind the other in a flow, an obvious concern is interference between them and the resulting error in the measurements. In this experiment, shock waves from the lead hot wire and its supports, as well as the wake of the first wire, may strike the second wire. However, the spectrum of the second wire did not exhibit any unexpected resonance or spikes, and the r.m.s. profiles of the fluctuations from the two hot wires proved comparable. Thus, it appears that the shock structure and wake emanating from the first hot wire and its supports had little effect on the active element of the second wire. The peak correlation between the two signals was nearly equal to 0.9 across the entire boundary layer, indicating the applicability of Taylor's hypothesis for small streamwise separations away from the wall.

The non-zero time delay corresponding to the peak of the space–time correlation, $\tau_{max}$, can be used along with the separation distance between the hot wires, $\xi_1$, to compute an average value of the convection velocity:

$$U_c = \frac{\xi_1}{\tau_{max}}.$$

The convection velocity calculated from the three different wire separations, normalized by the free-stream velocity, is shown along with a curve of the mean velocity profile in figure 3. Agreement between the runs is excellent, and apart from the points closest to the wall, the convection velocity appears to be nearly constant and equal to approximately $0.9U_\infty$ across most of the boundary layer. The discretization error caused by the analog-to-digital converter leads to an uncertainty in $U_c/U_\infty$ of $+0.09$, $-0.06$ for the smallest wire spacing and $+0.04$, $-0.05$ for the largest. There is very good agreement with the visual results of Smith & Smits (1988) in the same boundary layer, who showed that strong large-scale density structures travel at approximately $0.9U_\infty$, and with the results obtained by Tran (1987) using two wall-pressure transducers, who found $U_c \approx 0.9U_\infty$ with a streamwise separation of $4.0\delta$. Furthermore, the convection velocity determined for the individual large-scale structures using conditional sampling techniques is in good agreement with that measured here with a broadband technique (Donovan 1989; Spina 1988).

It should be noted that the broadband convection velocity may be dependent upon transducer separation, as shown by Owen & Horstman (1972) in a hypersonic

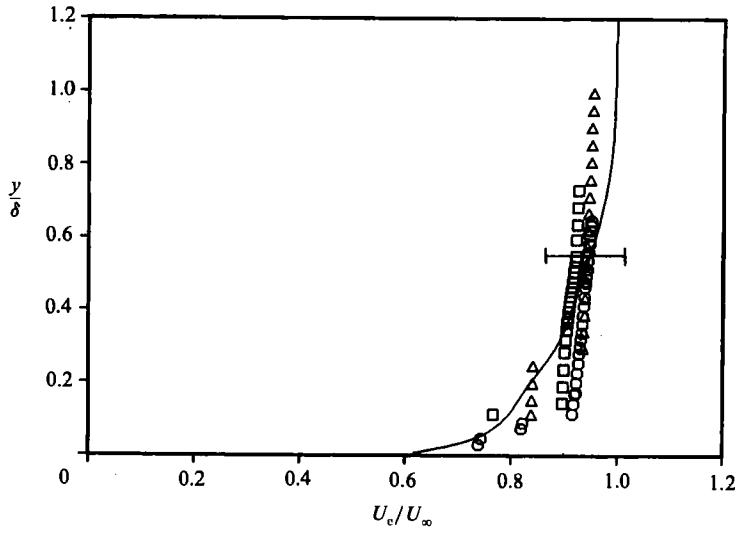


FIGURE 3. Broadband convection velocity, superimposed on the mean velocity profile; both are normalized by the free-stream velocity. The bar indicates the possible discretization error for the smallest wire spacing, which is the most sensitive to error. □, $\xi_1/\delta = 0.11$; ○, $\xi_1/\delta = 0.16$; △, $\xi_1/\delta = 0.18$.

boundary layer. This could be responsible for the variance between their convection velocity measurements and those from the present study. For $y/\delta > 0.3$, and with a streamwise spacing from $3.5$–$12.8\delta$, Owen & Horstman measured a range of convection velocities from 0.75 to $0.82U_\infty$. Nonetheless, it is significant that the convection velocity measured in this experiment is nearly constant across the outer part of the boundary layer, and this estimate ($U_c = 0.9U_\infty$) will be used throughout this paper.

### 3.2. *Vertical hot-wire separations*

Two hot wires with a fixed separation, one directly above the other, were traversed vertically across the boundary layer. The separation was varied from $0.09\delta$ to $0.60\delta$, with each wire spacing comprising a different experimental run. This extensive range of hot-wire separations allowed the vertical extent of the organized structures to be explored more thoroughly than by Spina & Smits (1987).

While this study traversed two probes with a fixed separation, most other measurements of this kind have used one detection probe fixed at the wall (hot wire, shear stress gauge, etc.) and another probe that was traversed through the boundary layer, thereby varying the separation between the wires. The present fixed-separation method was chosen to give a local measure of the inclination of the large-scale motions; the advantage of this method will be seen shortly. As a matter of convention, when dealing with vertically separated wires, the quoted $y$-position corresponds to the average location of the two wires.

When examining the simultaneous mass-flux traces for similarities, it was obvious that the upper hot wire detected common patterns before the lower wire, indicating the passage of large-scale motions inclined to the wall at an acute angle (see, for example, Spina & Smits 1987). This behaviour has been observed by many other researchers in subsonic flows, and a common way of characterizing the phenomenon is to quantify the angle at which the motions lean downstream. An average structure

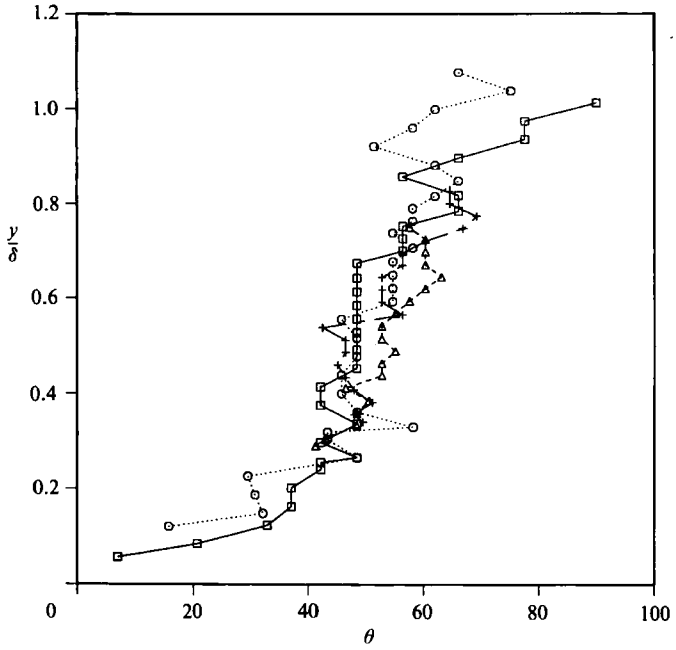


FIGURE 4. Average structure angle profiles for several vertical wire spacings. □——, $\xi_2/\delta = 0.09$; ○……, $\xi_2/\delta = 0.21$; △– – – –, $\xi_2/\delta = 0.30$; +—·—, $\xi_2/\delta = 0.40$.

angle, $\theta$, can be defined using the non-zero time delay from the distinct peak of the space–time correlation, $\tau_{max}$, the wire separation, $\xi_2$, and the convection velocity, $U_c$:

$$\theta = \tan^{-1}\left[\frac{\xi_2}{U_c \tau_{max}}\right].$$

The convection velocity found in the previous section, $0.9U_\infty$, was used throughout the boundary layer to determine $\theta$. It should be noted that this choice is not critical because a 10% change in $U_c$ will lead to a maximum difference in $\theta$ of less than 3°. While it is easy to conceptualize a large-scale structure leaning forward as it convects downstream, interpreting the structure angle as determined from two mass-flux signals is not a trivial task. As the conditional sampling results are presented and discussed in §4, the physical significance of the structure angle will become more evident.

It is important to emphasize that the cross-correlation gives a measure of the average turbulent scales – it is composed of contributions from a large variety of structures, no two of which are necessarily the same. Thus, the average structure angle is representative of a large number of individual large-scale structures, each inclined to the wall at its own angle and having its own strength. As mentioned previously, Spina & Smits (1987) found that the standard deviation of the individual structure-angle distribution is approximately 20°.

The average structure-angle profiles corresponding to wire separations ranging from $0.1\delta$ to $0.4\delta$ are plotted together in figure 4. The agreement is good, indicating that the average structure angle is only weakly sensitive to wire separation over a range of wire spacings. The structure angle deduced from wire separations of $0.5\delta$ and $0.6\delta$ follows the same trend shown; the scatter is larger, however. The characteristic

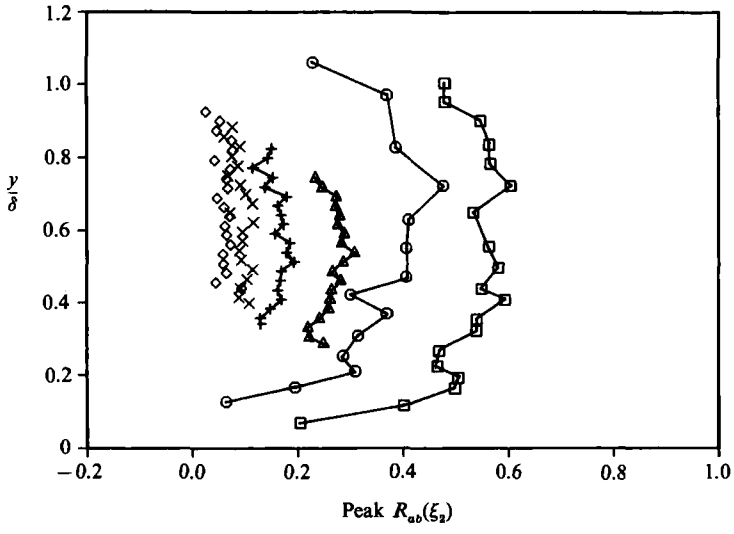


FIGURE 5. Peak values of the space–time correlations versus $y/\delta$ for each of the vertical hot-wire spacings. □, $\xi_2/\delta = 0.09$; ○, $\xi_2/\delta = 0.20$; △, $\xi_2/\delta = 0.30$; +, $\xi_2/\delta = 0.40$; ×, $\xi_2/\delta = 0.51$; ◇, $\xi_2/\delta = 0.60$.

structure angle is approximately 45–60° across much of the boundary layer. It is noteworthy that the average structure angle lies in this particular range, and it deserves some discussion because 45° is the angle usually associated with hairpin vortices in low-Reynolds-number boundary layers. Theodorsen (1952) was the first to suggest the existence and importance of horseshoe/hairpin vortical structures, as well as their characteristic inclination angle, 45°. Hairpins have been proposed as a major component of near-wall turbulence (Willmarth & Tu 1967; Offen & Kline 1975; Smith 1984 and others) and inner–outer interactions (Willmarth & Lu 1972; Black 1968; Robinson, Kline & Spalart 1988). Hairpin vortices have also been observed experimentally (Head & Bandyopadhyay 1981), and the dynamics of artificially-generated hairpins have been studied (Acarlar & Smith 1987). Because the measured structure angle in this flow is 45–60°, there is a tendency to attribute this phenomenon to the passage of hairpin vortices. While there may indeed be hairpin vortices in this supersonic boundary layer, there is no direct evidence for this conclusion. Rather, we can merely state that some characteristics of the motions are consistent with those of vortex-loop structures.

The peak values of the space–time correlations for each of the vertical hot-wire spacings are plotted versus mean wire position in figure 5. When $\xi_2 = 0.60\delta$, the correlation still has a small positive value, evidence that the largest organized structures span at least 60% of the boundary layer. The drop-off in peak correlation towards the wall could be caused by the diffuseness of the large-scale structures closer to the wall, a larger variation in individual structure angle near the wall, or simply by the increased variance of the mass-flux signals. Another possibility is that a distinct 'inner' organized structure smears the extensions of the large-scale structures closer to the wall. The diffuseness of the structures or the detection of inner-region motions could be the reason for the lower characteristic structure angle found by researchers using a probe fixed at the wall: Brown & Thomas (1977) found 18°, Rajagopalan & Antonia (1979) found 12.5°, while Robinson (1986*b*) found 16°. Conversely, Alving & Smits (1988) used the fixed-wire-separation method employed

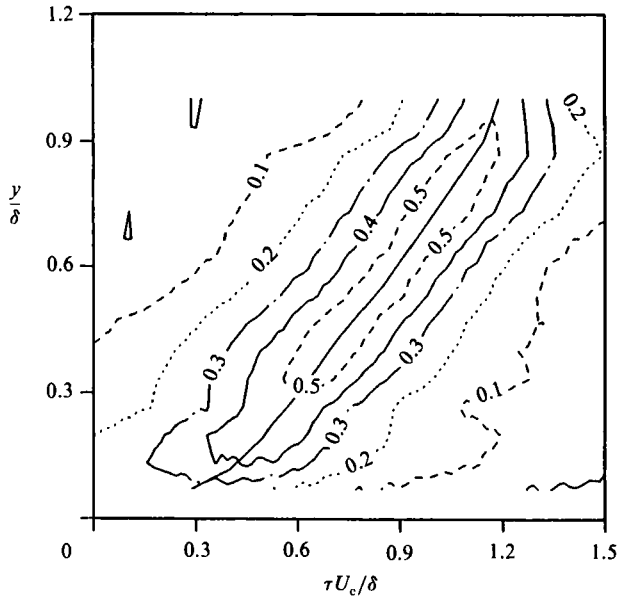


FIGURE 6. Equi-value space–time correlation contours from two hot wires with a vertical separation of $0.09\delta$.

here in an incompressible boundary layer, and found average structure angles ranging from 30 to 50°.

Smits *et al.* (1989) compared the vertical-separation space–time correlation results from a supersonic boundary layer with those measured in a subsonic boundary layer by Alving & Smits (1988) ($M = 0.1$, $Re_\theta = 5000$). Despite the use of the same measurement technique (fixed-probe separation) and similar peak values, the character of the correlations is quite different. For example, the correlation functions for the supersonic boundary layer are narrower than for the subsonic boundary layer (i.e. the correlation computed from the subsonic data decreases to a specified level in a longer non-dimensional time). Additionally, the structure angles measured by Alving (1988) in the low-speed flow are smaller than the comparable measurements in the supersonic boundary layer. This result may explain the differences observed in the correlation functions. Since the average large-scale structure is more upright in a high-Reynolds-number supersonic boundary layer, the extent of the structures in the mean flow direction will be smaller, and the space–time correlation is apt to fall off at shorter time delays. Since these two flows have such disparate Mach numbers (0.1 and 2.9) and Reynolds numbers ($Re_\theta$ of 5000 and 81000), it is not presently known whether these differences are due to compressibility or Reynolds-number effects.

Isocorrelation contours are a physically useful method for presenting space–time correlations. Using vertically separated wires, information on both vertical and streamwise extent of the average structure can be determined if Taylor's hypothesis is invoked. A superposition of correlation curves with the peaks lying on the 'mean structure shape' was used to produce the contour shown in figure 6 for $\xi_2 = 0.09\delta$. The mean structure shape, the solid curve drawn through the centre of the contours, was constructed from the mean structure-angle distribution across the boundary layer. Each cross-correlation curve was shifted to align the peak with the curve

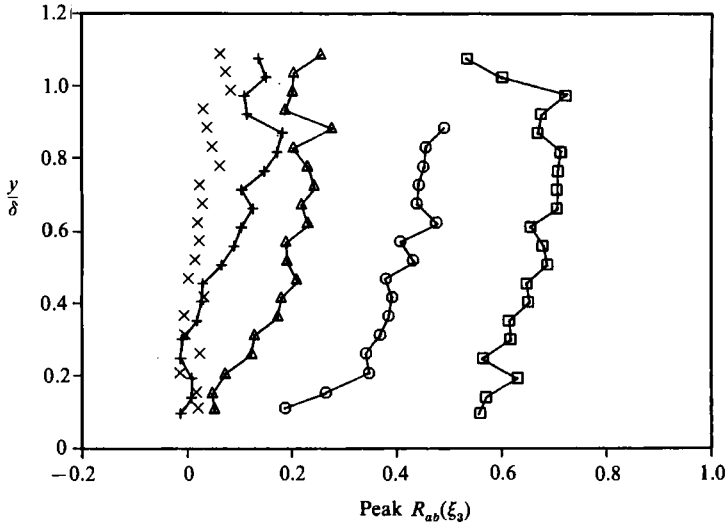


FIGURE 7. Peak values of the space–time correlations versus $y/\delta$ for each of the spanwise hot-wire spacings. □, $\xi_3/\delta = 0.09$; ○, $\xi_3/\delta = 0.14$; △, $\xi_3/\delta = 0.24$; +, $\xi_3/\delta = 0.37$; ×, $\xi_3/\delta = 0.54$.

delineating the mean structure shape. The contours give a good indication of the extent of the field around the average structure. The same mean structural characteristics are evident in the contours from each of the wire separations used in the present study, as well as in Robinson's (1986*a*) study of a supersonic boundary layer. In addition, the contours are similar to those measured by Kovasznay *et al.* (1970) in an incompressible flow.

### 3.3. *Spanwise hot-wire separations*

Two vertically-oriented hot wires were separated by a variety of spanwise spacings and traversed through the boundary layer. The spanwise wire separation was varied from $0.09\delta$ to $0.54\delta$, each separation comprising a different run. This hot-wire configuration enabled the spanwise lengthscale of the large-scale structures to be examined and contrasted with the vertical lengthscale determined in the previous section.

Correlations were computed for the entire range of spanwise spacings, and are similar in character to those found for the vertical separations (see Spina & Smits 1987), except that the peak occurs at zero time delay. The peak correlation values through the boundary layer are depicted in figure 7. Assuming that phase jitter affects the spanwise and vertical correlations equally, it appears that the spanwise extent of the large-scale structures is slightly less than the vertical extent. Evidence for this is the non-zero correlation for a vertical separation of $0.6\delta$ and the zero correlation for a spanwise separation of $0.54\delta$. The peak value of the correlation for each spanwise separation increases with distance from the wall, which could be due to the existence of distinct smaller-scale motions closer to the wall. Since the probes do not approach the inner layer, it is more likely that the large-scale structures which contribute to the correlation simply become wider as $y/\delta$ increases. The notion that the detected motions become wider with $y/\delta$ is consistent with both Townsend's 'attached eddy hypothesis' and mixing length theory. This also helps to explain why Spina & Smits observed a limited spanwise extent when correlating a wall-pressure

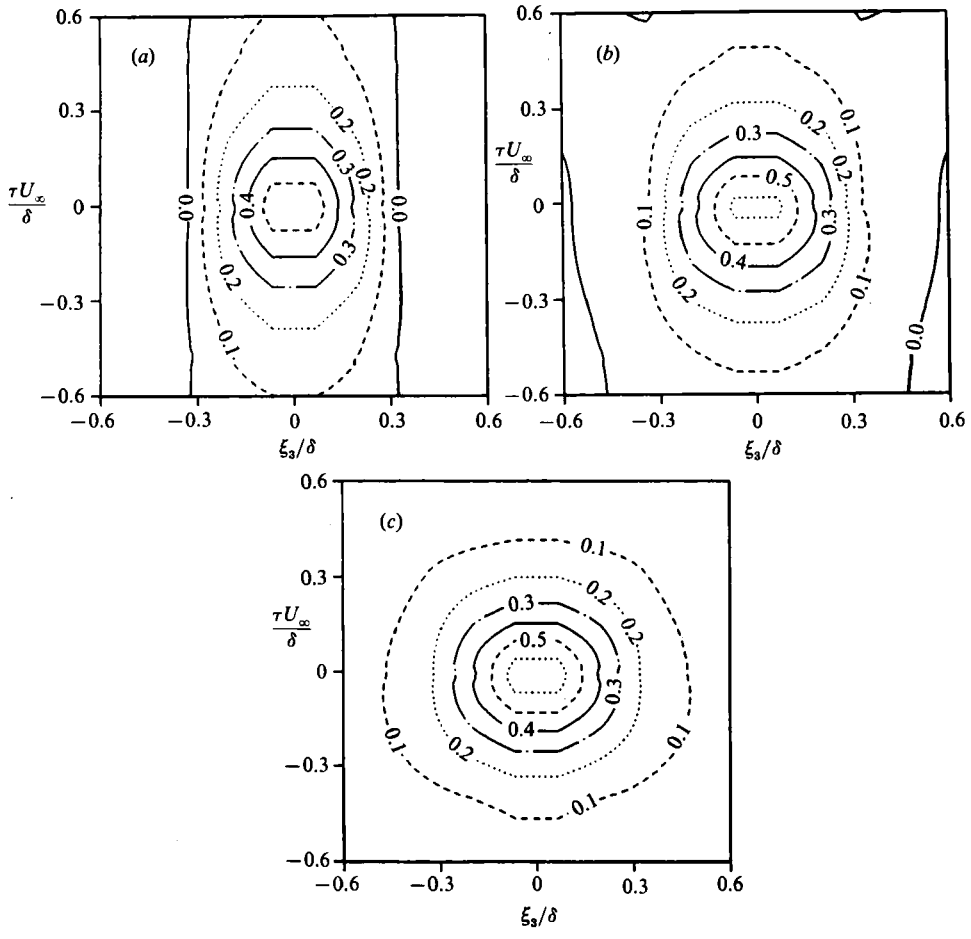


FIGURE 8. Equi-value space–time correlation contours generated using spanwise wire separations at: (*a*) $y/\delta = 0.20$, (*b*) $y/\delta = 0.51$, (*c*) $y/\delta = 0.82$.

signal with a hot-wire signal. Since the pressure transducers are at the wall, the narrowest region of the structures was sensed.

The transverse scales were further explored with the aid of isocorrelation contours, enabling the behaviour of the entire correlation curve to be observed, not just the peak value. Contours were constructed from the space–time correlations for all five spanwise separations at three different hot-wire pair locations: $y/\delta = 0.20$, 0.51, and 0.82 (Figure 8). To aid in interpretation, the correlations were reflected about the zero-separation line (valid since the mean spanwise correlations are symmetric in the $(y, z)$-plane). The time delay was normalized by outer-layer variables, and can be interpreted as a streamwise distance using Taylor's hypothesis. The contours can then be considered as a top-view ($x$–$z$ cross-sections) of the average organized structure at three different heights in the boundary layer. The difference in the spanwise extent of the large-scale structures across the boundary layer is clearly revealed by figure 8, reinforcing the earlier conclusion that the spanwise scale of the detected structures increases away from the wall. This is easily seen by examining the spanwise extent of a single contour line at zero time delay, say $R_{ab} = 0.10$, which is found to extend $\sim 0.3\delta$ at $y = 0.20\delta$, $\sim 0.35\delta$ at $y = 0.51\delta$, and $\sim 0.48\delta$ at $y =$

$0.82\delta$. Kovasznay *et al.* (1970) produced a similar contour picture in incompressible flow at $y/\delta = 0.50$, and the spanwise extent which they measured is in excellent agreement with that observed at the same location in the present study.

### 3.4. *Summary of two-point correlation results*

The two-point correlation techniques provided a useful insight into the average characteristics of large-scale structures in supersonic boundary layers. The vertically separated mass-flux measurements revealed the oft-observed downstream-leaning characteristic of the large-scale structures, and their characteristic angle of inclination was found to be 45–60° for $0.2 < y/\delta < 0.8$. The vertical scale of the largest structures was found to be at least $0.60\delta$. The spanwise scale of the structures which contribute to the correlation was slightly less than the vertical, and was found to increase with distance from the wall. Finally, the broadband convection velocity was uniform across 80% of the boundary layer, suggesting that a large-scale structure convects with one speed, about 10% less than the free-stream velocity.

## 4. Conditional sampling of normal hot-wire signals

The VITA conditional sampling technique, described in detail by Blackwelder & Kaplan (1976), was used to extract specific information concerning the characteristics and kinematics of the organized structures. The VITA technique detects segments of a fluctuating signal where the local derivative is elevated, implying the presence of a sharp gradient in the flow.

### 4.1. *Interpretation of existing VITA results in supersonic flows*

The conditional sampling results from normal hot wires in supersonic boundary layers presented by Robinson (1986*a*) and by Spina & Smits (1987) provided a preliminary analysis of organized motions in compressible flows. Most importantly, they showed that VITA successfully detects steep streamwise mass-flux gradients in compressible boundary layers, and that large positive mass-flux gradients are significantly more numerous than large negative mass-flux gradients. Spina & Smits and Robinson used multiple vertically separated normal wires to show that the strong positive gradients detected with VITA extend over most of the boundary-layer thickness. They also found that the structure angles determined from average and individual positive VITA events are in excellent agreement with the structure angles determined by the cross-correlation method, implying that the positive streamwise mass-flux gradients are the primary contributors to the peak of the vertical cross-correlation. This is not surprising, since it is clear from a visual examination of the signals from vertically-separated normal wires (see figure 15 in Spina & Smits) that the strong positive mass-flux gradients are the doiminant feature of the time histories.

The strength, vertical extent, and dominance of the mass-flux gradients discussed above suggests that the strong positive VITA (+VITA) events correspond to the upstream edge of large-scale turbulent bulges. This notion is consistent with the shape of both individual and average +VITA events, which begin with the streamwise mass flux gradually decreasing below the mean. This is immediately followed in time by a sharp, distinctive rise in the mass flux, which could correspond to the upstream interface of the structure (the 'back' of the turbulent bulge), where the high-momentum fluid entrained from the free stream meets the low-momentum fluid contained within the organized motion.

Direct evidence for the correspondence of strong + VITA events with the upstream interfaces of large-scale structures comes from Smith (1989), who performed a series of simultaneous flow visualization and hot-wire measurements in this same boundary layer. Smith observed strong positive-density-gradient structures (similar to those shown in figure 1) which possessed hot-wire traces similar to the positive VITA events. Although the experiment was not able to establish a one-to-one correspondence (because of the optical integration of schlieren), Smith's results lend some support to the idea that the sharp gradients detected by + VITA correspond directly to the sharpest density (and hence streamwise velocity) gradients in the flow – those at the upstream edge of the organized motion.

Thus, it appears that the dominant measurable characteristic of large-scale organized structures in supersonic flow (a strong streamwise mass-flux/velocity gradient) is the same feature seen by many researchers in incompressible flow, and that this trait can be detected as a positive VITA event. The structural characteristic represented by the negative VITA event is not as clear. While an obvious possibility is the leading edge (downstream interface) of the structure, there is no direct evidence to support this in supersonic flow. The negative events have a lower frequency content and are more diffuse than the positive events, and in incompressible flow these traits have been attributed to the downstream interface of organized structures.

## 5. Conditional sampling of crossed-wire signals

In this section, both VITA and Quadrant conditional sampling results are presented based on the two flow components measured by a crossed wire in supersonic flow, $(\rho u)'$ and $v'$, and their product, $(\rho u)'v'$. The Quadrant technique (Wallace, Eckelmann & Brodkey 1972; Willmarth & Lu 1972) detects regions of high contribution to the Reynolds stress by thresholding the highly intermittent $(\rho u')v'$ signal, and then classifies the motions according to the signs of $(\rho u)'$ and $v'$. The relation between the incompressible Reynolds stress and the 'density-weighted' shear stress which a crossed-wire probe responds to is addressed in Appendix B.

The high probability of correspondence between the upstream edge of large-scale organized structures and positive VITA events (discussed in §4) is relied upon in this analysis to identify the kinematics of the flow field within and upstream of the structures. To this end, various methods for determining the flow field in the vicinity of a structure are triggered by the detection of a strong positive VITA event in the streamwise mass flux. To ensure the equivalence of a + VITA event with the occurrence of a dominant large-scale organized structure, elevated + VITA thresholds were used in this analysis, ranging from $k_\nu = 1.0$ to 1.5.

VITA and Quadrant conditional sampling were performed simultaneously on the crossed-wire signals. Portions of the three signals at $y/\delta = 0.54$ are shown in figure 9 along with a time-line illustrating the location and duration of the detected VITA ($k_V = 0.8$) and Quadrant ($k_Q = 2.0$) events. There appears to be a correspondence between some of the positive VITA events and significant shear product† activity (e.g. the third and fourth + VITA events). This behaviour will be explored in §5.3, where the percentage of + VITA events associated with Quadrant events will be quantified. First, however, the independent application of VITA and Quadrant conditional sampling on the crossed-wire signals will be discussed.

† The 'shear product' is defined here as $(\rho u)'v'$; this can be loosely interpreted as the 'instantaneous density-weighted shear stress'.

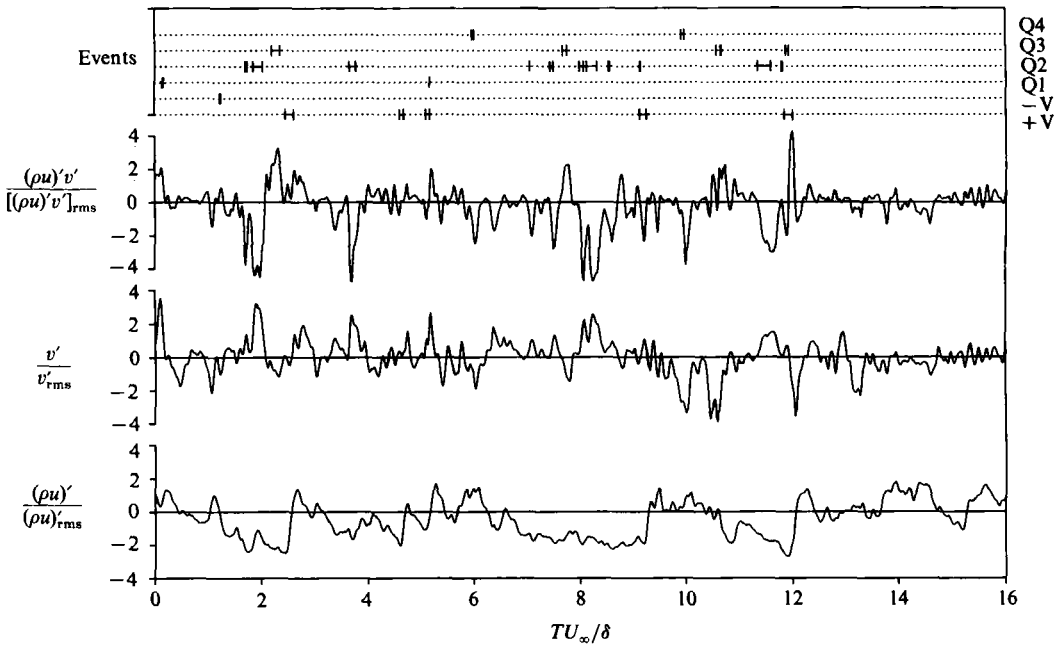


FIGURE 9. Segments of the three crossed-wire signals along with a time-line of the detected VITA and Quadrant events ($k_V = 0.8$, $k_Q = \pm 2.0$).

### 5.1. *Independent application of Quadrant and VITA*

With the Quadrant technique, ensemble averages of the events in each quadrant are calculated. The Quadrant 2 ensemble averages of $(\rho u)'$, $v'$, and $(\rho u)'v'$ are shown in figure 10, where a threshold of twice the r.m.s. of $(\rho u)'v'$ was used. The $(\rho u)'v'$ ensemble average is characterized by rather narrow spikes throughout the boundary layer. The $v'$ ensemble averages are highly correlated (negatively correlated for Quadrant 2) and in-phase with the shear product spikes, while the $(\rho u)'$ ensemble averages are somewhat broader and not as well defined. The general characteristics exhibited by each of the Quadrant 2 ensembles appear in the ensemble averages for all quadrants (not shown here). In particular, the signatures are relatively invariant with position in the boundary layer, and while the $(\rho u)'v'$ and $v'$ ensembles are correlated, the $(\rho u)'$ average is more diffuse.

Figure 11 illustrates the number of detected Quadrant events through the boundary layer for $k_Q = \pm 2.0$. The most frequently occurring motion contributing to $-\overline{(\rho u)'v'}$ near the wall is that of quadrant 4 (Q 4). As the boundary-layer edge is approached, the frequency of occurrence of Q 4 motions diminishes, while that of Q 2 motions increases. These contributions to the Reynolds shear stress are indicative of 'cross-gradient mixing' in the boundary layer (Robinson 1989). The negative shear-stress motions, Q 1 and Q 3, occur less frequently than the Q 2 and Q 4 motions. The overall distribution of Quadrant events across this high-Reynolds-number supersonic boundary layer is similar in character to that found in incompressible, low-Reynolds-number boundary layers as shown by the quadrant analysis of Alving (1988).

In §4, +VITA events were found to correspond to steep streamwise mass-flux gradients which extend over significant fractions of the boundary-layer thickness and are inclined at an angle of roughly 50° to the wall. The crossed-wire data can be used to determine the behaviour of the normal velocity, $v'$, and the shear product,

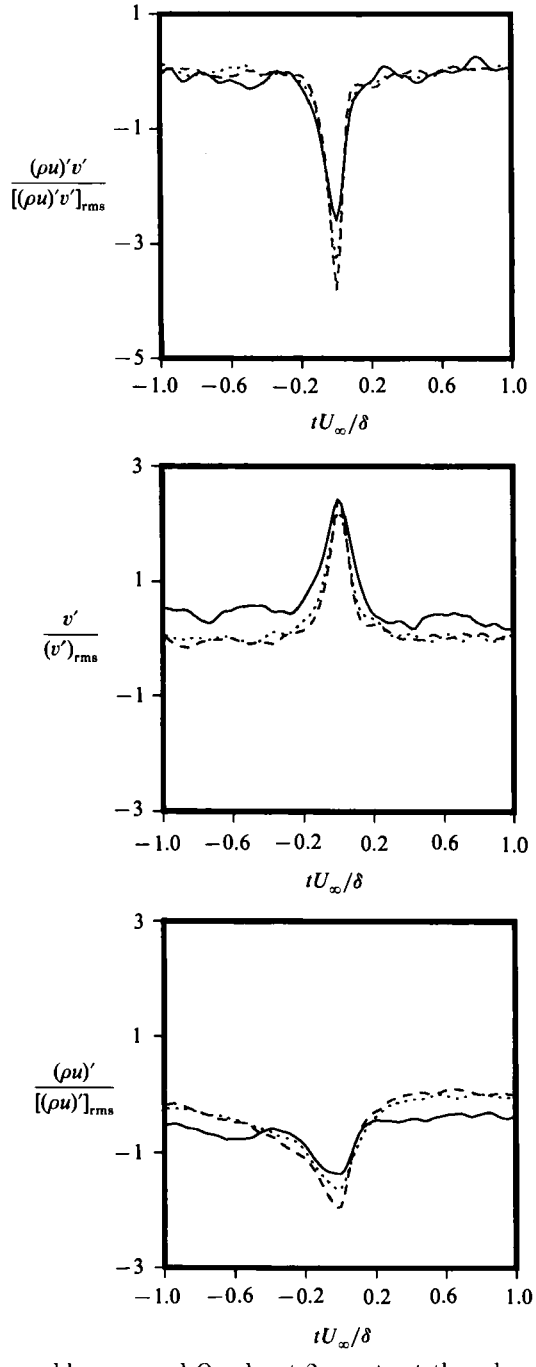


FIGURE 10. Ensemble-averaged Quadrant 2 events at three locations in the boundary layer. ——, $y/\delta = 0.2$; ....., $y/\delta = 0.5$; – – –, $y/\delta = 0.8$.

$(\rho u)' v'$, during the passage of these streamwise mass-flux fronts. To this end, the short-time variance of $(\rho u)'$ was used as the detection signal for $(\rho u)'$, $v'$, and $(\rho u)'v'$. Thus, when an event was detected based on the short-time variance of $(\rho u)'$, portions of each signal in the region of detection were accumulated and averaged independently.

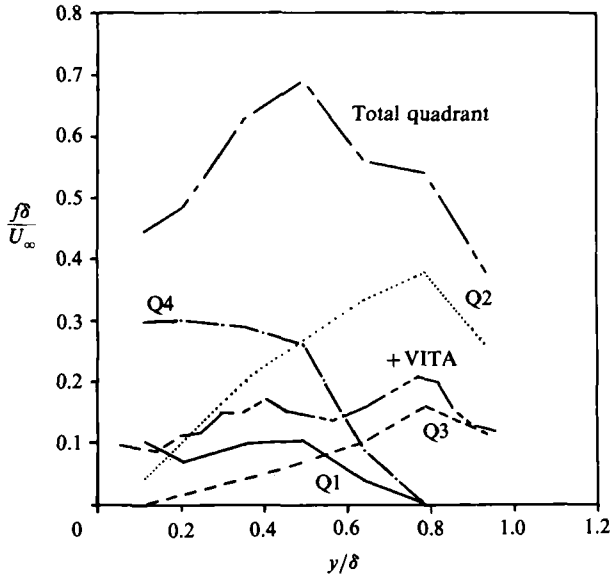


FIGURE 11. The normalized frequency of occurrence of detected Quadrant events as a function of $y/\delta$ ($k_Q = \pm 2.0$). The frequency of positive VITA events is also shown for reference ($k_V = 1.1$).

The resulting ensemble-averaged signatures are shown in figure 12 for three positions in the boundary layer. Some of the characteristics of the $(\rho u)'$ conditional average are functions of position in the boundary layer. Near the wall ($y/\delta = 0.2$), the sharp streamwise mass-flux gradient in the centre of the event is followed by a significant positive excursion from the mean and preceded by a small 'deceleration'. In contrast, at $0.8\delta$ the sharp $(\rho u)'$ gradient is preceded by a large negative peak and followed by a small positive peak. The $v'$ conditional average, $\langle v' \rangle$, is not as distinct as $\langle (\rho u)' \rangle$, indicating some jitter in the phase relationship between $(\rho u)'$ and $v'$ during +VITA events. However, distinct negative gradients in $\langle v' \rangle$ are associated with the detected positive gradients in $\langle (\rho u)' \rangle$. The character of $\langle v' \rangle$ is also a function of $y/\delta$, as the largest peak is negative at $0.2\delta$ and positive at $0.8\delta$. Furthermore, the negative peak of $\langle v' \rangle$ at $0.2\delta$ is in-phase with the large positive peak of $\langle (\rho u)' \rangle$ occurring after the streamwise mass-flux gradient, and the positive peak of $\langle v' \rangle$ at $0.8\delta$ is in-phase with the negative peak of $\langle (\rho u)' \rangle$ occurring before the gradient. Thus, +VITA detects sharp streamwise mass-flux gradients which are associated with significant contributions to the Reynolds shear stress, as seen in the ensemble average of the shear product (see §5.4 for further discussion of this point). It also confirms that the primary contribution to the shear stress in the lower part of the boundary layer is from Q 4 events ($+(\rho u)'$ and $-v'$ peaks are coincident), while Q 2 events are dominant in the upper part of the boundary layer ($-(\rho u)'$ and $+v'$ peaks are coincident). It is clear that towards the middle of the boundary layer, where both Q 2 and Q 4 events are important, great care must be taken when interpreting the conditional averages. The existence of two shallow peaks in the shear product ensemble average at $0.5\delta$ is most probably an artifact from the averaging of Q 2 and Q 4 events.

Thus far, two different conditional sampling techniques have been used to detect motions in the boundary layer. The techniques are based upon different detection criteria, and therefore the ensemble averages obtained with the two methods are different. An important question is: 'How are the two different signatures related?'

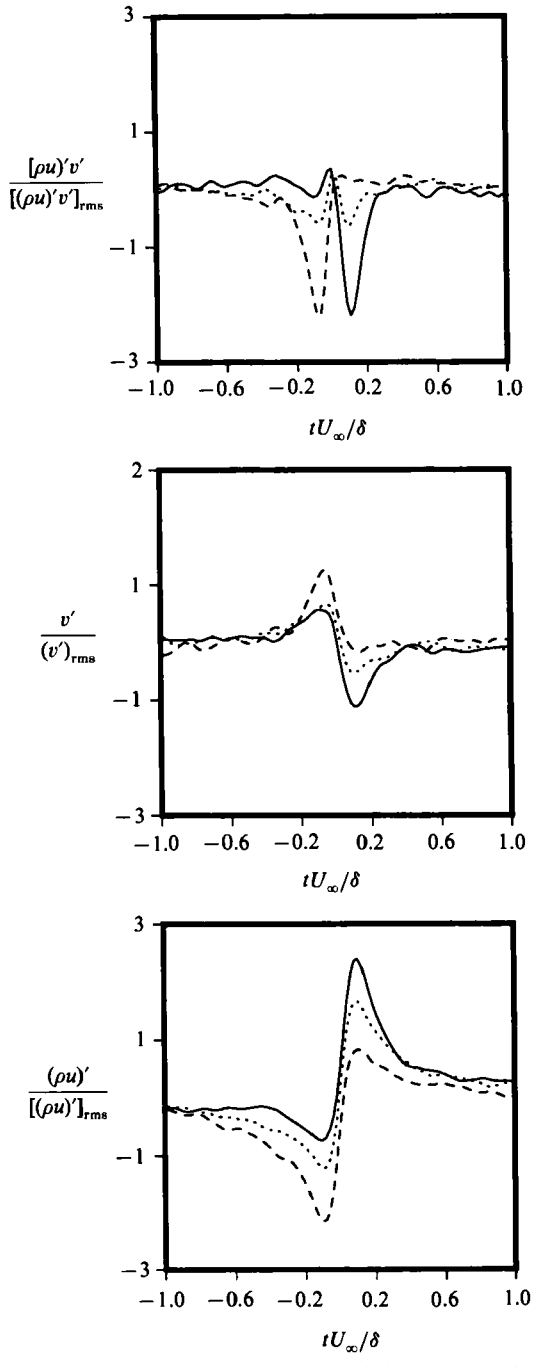


FIGURE 12. Ensemble-averaged $(\rho u)'$, $v'$, and $(\rho u)'v'$ signatures based upon the positive VITA technique (detection on $(\rho u)'$). ——, $y/\delta = 0.2$; ....., $y/\delta = 0.5$; – – –, $y/\delta = 0.8$.

Clearly, there is some degree of correspondence between the techniques, since the VITA criterion yields events which are associated with large negative spikes in the instantaneous shear product at several locations in the boundary layer. Near the wall the +VITA ensemble average has a strong Q 4 motion after the event centre, and

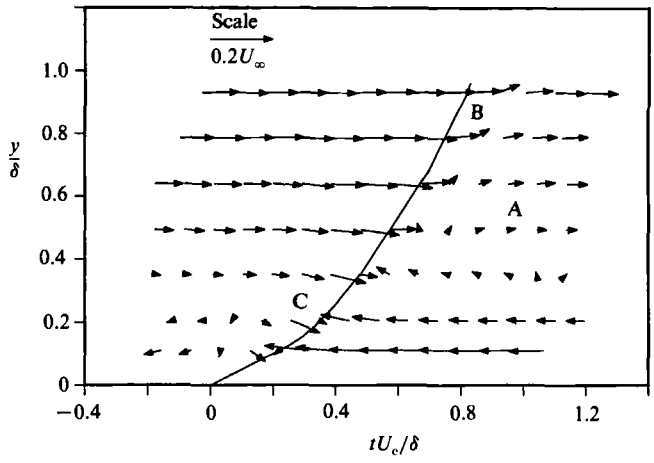


FIGURE 13. Ensemble-averaged flow field upstream and downstream of +VITA events, in a reference frame moving with the convection velocity of the large-scale motions. The number of events in the ensemble ranges from 69 events at $0.2\delta$ to 259 events at $0.8\delta$.

near the edge of the boundary layer a strong Q 2 motion occurs before the event centre.

### 5.2. *The ensemble-averaged structural flow field detected with VITA*

Since the streamwise mass-flux fronts detected with +VITA are assumed to extend across a large portion of the boundary layer, as hypothesized in §4, then the crossed-wire signals can be used to determine the ensemble-averaged, two-dimensional flow field associated with the structure. Using Taylor's hypothesis, the +VITA $\langle(\rho u)'\rangle$ and $\langle v'\rangle$ signatures can be interpreted as a spatial cut through the ensemble-averaged flow field. The fluctuating quantities used to determine the VITA ensemble averages are relative to the local mean, so the difference between the local mean and the assumed convection velocity, $0.9U_\infty$, was added to the ensemble-averaged velocities at each location. This yields a velocity field relative to a reference frame convecting with the mass-flux gradient. To achieve the correct spatial relationship, the VITA events were shifted to align their centres with the mean structure shape derived from the measurement of the structure angle. When constructing the resultant velocity vectors from $u'$ and $v'$, positive VITA events were used across the boundary layer, even though the difference between the convection velocity and the local mean velocity changes sign at approximately $0.3\delta$. The Strong Reynolds Analogy (SRA) was used to convert $(\rho u)'$ to $u'$, leading to a possible error in $u'$ of approximately −14% to +24% (see Smits & Dussauge 1989).

The resulting velocity field is shown in figure 13 for the positive events, corresponding to the upstream side (back) of a turbulent bulge. The free-stream velocity is from left to right and the mean structure shape is indicated on the plot. The figure depicts the velocity field which would be observed if convecting with the upstream interface of the ensemble-averaged structure. Note that the velocity vectors shown at the structure-shape line have a non-zero streamwise component. This is due to several factors, including the small difference between the actual convection velocity and the value used for $U_c$, errors in $u'$ due to use of the SRA, and the arbitrary location of the VITA event centre, which is based upon a maximum in the short-time variance. However, the overall trends of the ensemble flow field associated with the sharp streamwise mass-flux gradient seem to be captured by this technique.

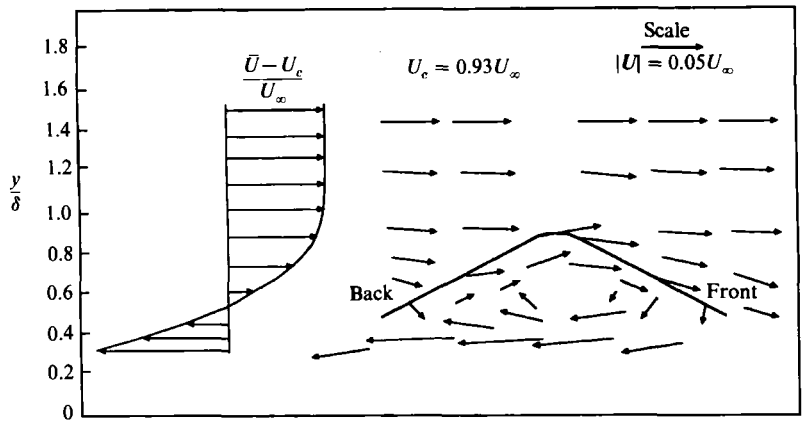


FIGURE 14. Schematic of a large-scale turbulent 'bulge' in incompressible flow; Blackwelder & Kovasznay (1972).

As expected, the upstream edge of the structure appears as an interface between high-speed fluid upstream and low-speed fluid downstream. The low-speed region within the bulge rotates on a large scale in the direction of the mean shear (region A in figure 13). Just downstream of the interface, in the outer portion of the boundary layer, the high-speed fluid appears to flow over the low-speed rotating region (region B), but lower in the boundary layer the high-speed fluid approaching the bulge turns towards the wall (region C). This behaviour suggests the presence of a saddlepoint occurring on the upstream face of the structure at approximately $0.6/0.7\delta$. From the orientation of the velocity vectors, it is evident that the flow field must be strongly three dimensional to satisfy continuity. This flow field, including the saddle point, is similar to that proposed by Kovasznay *et al.* (1970), Blackwelder & Kovasznay (1972) (see figure 14), Brown & Thomas (1977), and Falco (1977) for a turbulent bulge in an incompressible flow.

### 5.3. *The instantaneous structural flow field detected with VITA*

In §5.2 an ensemble-averaged picture of the flow field associated with the sharp streamwise mass-flux gradients was presented. However, interpreting ensemble-averaged signals as being representative of actual motions in the flow is not always correct. For example, Fernando *et al.* (1987*b*) noted that the VITA averaging procedure may group two or more different types of positive mass-flux gradients together, thereby generating a non-representative ensemble average. This possibility is confirmed by figure 12 (at $y/\delta = 0.5$), where the detection of +VITA $(\rho u)'$ events has grouped Q 2 and Q 4 shear stress events together to obtain a misleading shear product ensemble average.

In this section, the validity of the ensemble-averaging procedure in representing actual boundary-layer structures will be investigated. A search was conducted for individual motions which possess characteristics similar to those exhibited by the ensemble flow field. This search was performed using VITA and Quadrant detection simultaneously on the signals obtained from the crossed-wire probe.

#### 5.3.1. *Double event patterns*

Strong +VITA events detected in the streamwise mass-flux signal ($k_V = 1.1$) were used to trigger the Quadrant conditional sampling technique. Each of the four thresholded Quadrant motions was examined separately so that any temporal or

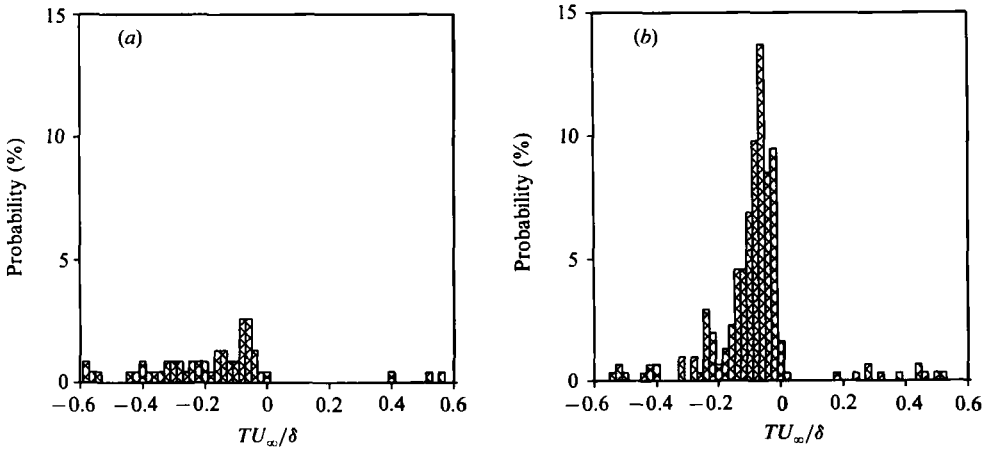


FIGURE 15. Histograms of the time between detection of a +VITA event and the detection of a Q 2 event. The ordinate is the percentage of +VITA events which have a Q 2 event downstream ($-T$) or upstream ($+T$). (*a*) $y/\delta = 0.33$, (*b*) $y/\delta = 0.77$.

phase relationship with the +VITA event could be discovered. A histogram of time delays between event detections was constructed at each point in the boundary layer, for each possible 'pair', to determine whether a specific Quadrant event consistently leads or lags a +VITA event. The trends will be presented in terms of the percentage of +VITA events possessing a particular pattern, since it is assumed that the +VITA events identify a large-scale structure.

Because a +VITA event corresponds to a transition from low-momentum fluid to high-momentum fluid, a +VITA event will be preceded in time by either Q 2 or Q 3 motions and followed by either Q 1 or Q 4 motions. These trends were observed for thresholded (high-intensity) shear stress events, however, making the combinations more significant. The four observed patterns were:

2V. Positive VITA preceded by a Quadrant 2 event (Q 2→+V);
3V. Positive VITA preceded by a Quadrant 3 event (Q 3→+V);
V1. Positive VITA followed by a Quadrant 1 event (+V→Q 1);
V4. Positive VITA followed by a Quadrant 4 event (+V→Q 4).

The histograms of the time between detection of a +VITA event and the detection of a Q 2 event (pattern 2V) are shown in figure 15 for $y/\delta = 0.33$ and 0.77 ($-T$ corresponds to a Q 2 event occurring before the +VITA event). This pattern occurs frequently near the outer edge of the boundary layer; nearly three-quarters of the +VITA events are preceded by a Q 2 event within $T^* = TU_\infty/\delta = 0.4$ at $y/\delta = 0.77$. The one-sidedness of the distributions testifies to the physical significance of the pattern. Histograms were constructed across the boundary layer for each of the patterns listed above, and where a pair occurred, the distribution was one-sided.

The trends are summarized in figure 16, which shows the percentage of +VITA events in each of the patterns. Since the number of realizations of each pattern follows the same trend as the number of detected Quadrant events seen in figure 11 (i.e. the number of Q 2 and Q 3 events increase across the boundary layer while the number of Q 1 and Q 4 decrease), the significance of the pattern variation across the

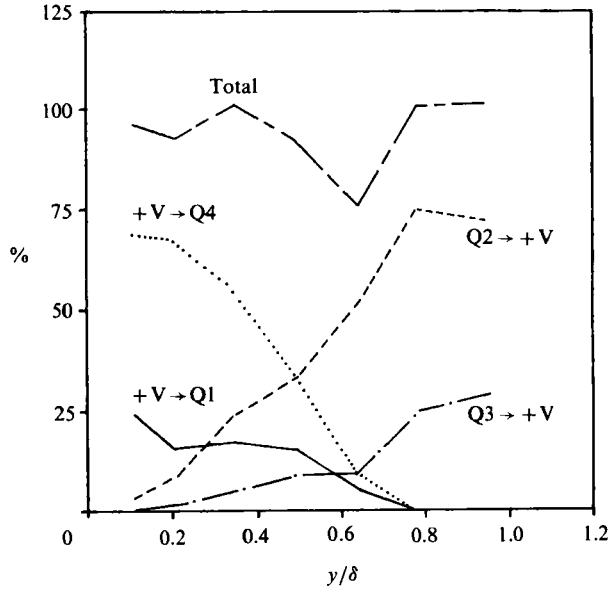


FIGURE 16. Percentage of +VITA events occurring in each of the double event patterns ($k_Q = \pm 2.0$, $k_V = 1.1$).

boundary layer was unknown at this point of the investigation. Until the motions were examined in the absence of a threshold, no conclusions could be made concerning where in the boundary layer each pattern dominates (see below). However, it is clear from this analysis that distinct regions of intense shear stress are associated with the turbulent bulges which the +VITA technique detects: Q 2 and Q 3 events occur downstream of the structure, and Q 1 and Q 4 events occur upstream of the structure. These relationships are consistent with the ensemble-averaged flow field revealed in §5.2 and illustrated in figure 13.

### 5.3.2. *Triple event patterns*

To further explore the validity of the ensemble-averaged flow field, a search was conducted for patterns composed of 'triple events'; that is, a +VITA event with shear stress events on both sides. Because of the one-sidedness of the double-event distributions, only four distinct triple-event patterns are feasible (see figure 17 for a schematic of each pattern):

3V1. +VITA with a Quadrant 3 event downstream and a Quadrant 1 event upstream
(Q 3→+V→Q 1);

3V4. +VITA with a Quadrant 3 event downstream and a Quadrant 4 event upstream
(Q 3→+V→Q 4);

2V1. +VITA with a Quadrant 2 event downstream and a Quadrant 1 event upstream
(Q 2→+V→Q 1);

2V4. +VITA with a Quadrant 2 event downstream and a Quadrant 4 event upstream
(Q 2→+V→Q 4).

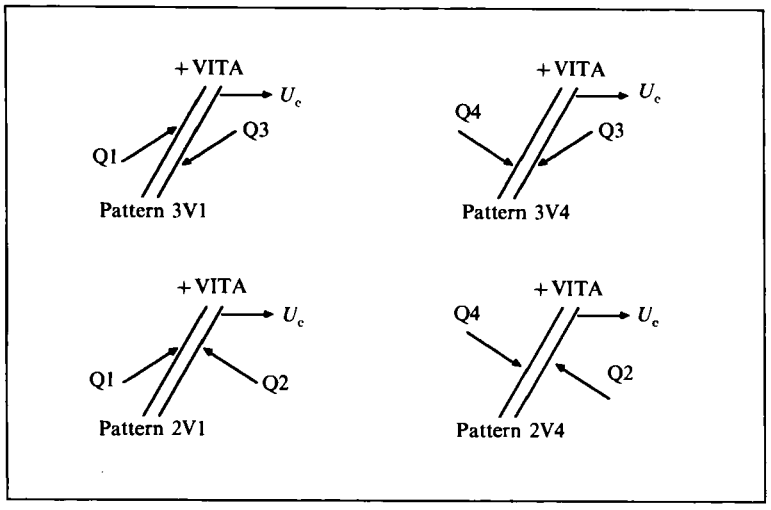


FIGURE 17. Schematic of the four possible triple event patterns showing the spatial location of the shear stress events relative to the +VITA event.

The same method used to detect double events was applied to detect triple events, with the addition of another search window. When the same windows and thresholds were used for triple-event detection as had been employed to detect double events, the percentage of +VITA events categorized as triple events was minimal, with a maximum of 7% for any of the four patterns. To increase the number of detected triple events, the detection thresholds were adjusted. The new thresholds were: $k_V = 1.5$, for detection of very strong +VITA events, which have a higher probability of direct correspondence with the upstream edge of an organized structure, and $k_Q = 1.8$, for the admission of slightly weaker shear stress events. At $y/\delta = 0.77$, no triple events were detected because of the lack of Q 1 and Q 4 events there.

The percentage of +VITA events which are part of each of the four possible triple event patterns is shown in figure 18 versus $y/\delta$ for a window of $T^* = 0.40$ on each side of the +VITA events. Also indicated on this plot is the percentage of +VITA events which are associated with all of the triple-event patterns together, which reaches a maximum of 50%. This correspondence between strong +VITA events and thresholded shear stress events both upstream and downstream, although low, is still evidence of the significance of the +VITA events and the relation of +VITA events to elevated levels of the shear product. As for the relative importance of the four different triple event patterns, the two patterns with Q 2 events within the structure (i.e. patterns 2V1 and 2V4) occur more frequently than structures with Q 3 events inside (patterns 3V1 and 3V4), and thus seem to be more characteristic of the flow. This was also the case for the ensemble-averaged flow field constructed solely from the +VITA events seen in figure 13. The two patterns involving Q 3 events consistently account for less than 8% of the positive VITA events.

At first glance, the structures associated with Q 2 events seem evenly distributed between those followed by Q 4 events (pattern 2V4) and those followed by Q 1 events (pattern 2V1). A subtle, but nevertheless important, difference is seen by closely examining these two patterns. Lower in the boundary layer, $y/\delta = 0.33$, the structures followed by Q 4 are dominant, while every position above that point shows that the structures are more often followed by Q 1 than Q 4 events. Again

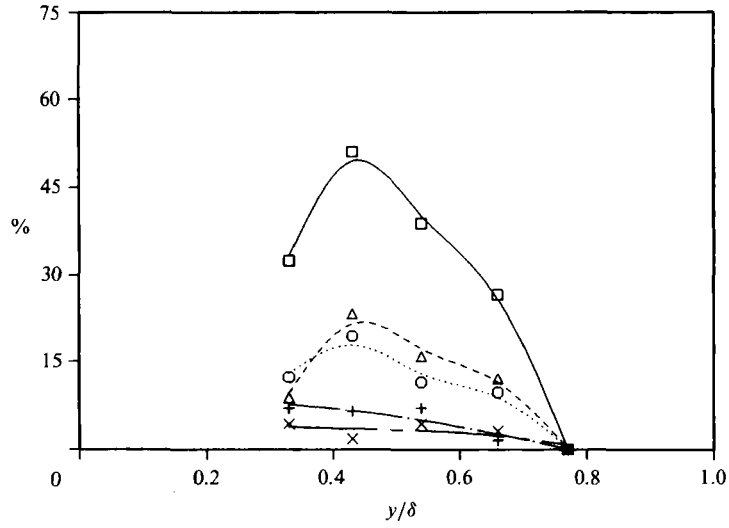


FIGURE 18. Percentage of +VITA events occurring in each of the triple event patterns defined by thresholding the shear stress. □——, Combined; ○....., 2V4; △----, 2V1; +—·—, 3V4; ×—·—, 3V1.

consistent with the ensemble-averaged flow field, this result suggests that the sharp interface demarcating the back of the organized structure is followed by high-momentum, downward motions in the lower part of the boundary layer, and high-momentum, upward motions in the upper region of the boundary layer. This behaviour is similar to that found for incompressible, low-Reynolds-number boundary layers by Brown & Thomas (1977), Praturi & Brodkey (1978) and others experimentally, and by Robinson *et al.* (1988) in a computational boundary layer generated from a direct Navier–Stokes simulation.

The flow field upstream and downstream of a +VITA event has been defined to this point by the detection of thresholded shear stress events. While the Quadrant technique is very useful for detecting regions of high-intensity shear, it is perhaps too restrictive to determine the dominant trends near the upstream interface of the large-scale structures. In an attempt to eliminate the dependence of the resulting triple event patterns on the Quadrant threshold, a different method for detecting the primary motions on both sides of +VITA events was explored.

The algorithm for detecting triple events without thresholding the shear stress can be summarized as follows:

1. Detect +VITA events on the streamwise mass-flux signal ($k_V = 1.1$);

2. Choose a window on each side of the +VITA event which is representative of the timescales near the event within which the quadrant of each data point (i.e. the discrete data points sampled by the analog-to-digital converter) will be evaluated. The window chosen was $T^* = 0.30$, which corresponds to 15 data points ($N_w = 15$);

3. Define a number of points, $M$, so that when $M$ data points out of $N_w$ are in a specific quadrant, a 'trend' is defined for the motion on that side of the structure interface.

$M$ was chosen to be 10, so that if 67% of the data points on one side of the +VITA event were of the same shear product type, a trend would be defined. The resulting plot of percentage of +VITA events belonging to each of the four triple-event patterns is shown in figure 19 versus $y/\delta$. The kinematics of the large-scale structures

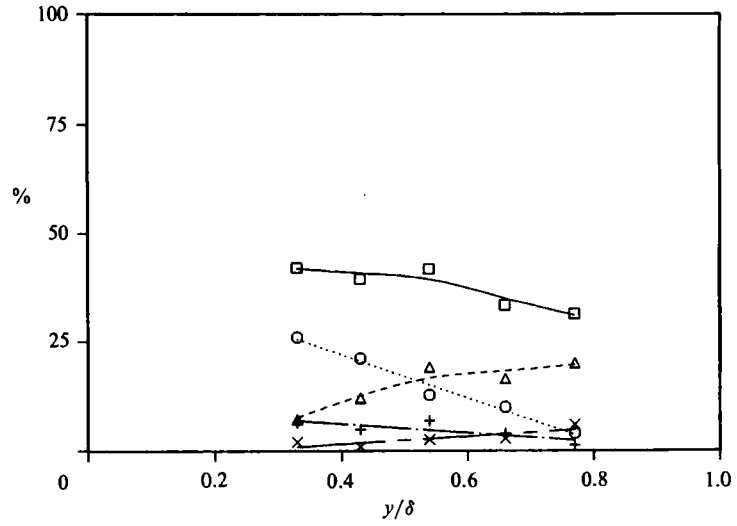


FIGURE 19. Percentage of +VITA events occurring in each of the triple event patterns defined by 'windows' (67% of the window defining a trend). □ ——, Combined; ○ ....., 2V4; △ – – –, 2V1; + — · —, 3V4; × — · —, 3V1.

first observed in the ensemble-averaged velocity field is clear. The total percentage of positive VITA events corresponding to triple-event patterns is significant across the boundary layer, ranging from 31–42%. Once again we see the dominance of the internal Q 2 motions over the Q 3 motions, although Q 3 motions occur within some structures.

Most significantly, the primacy of the 2V4 motions is established in the lower portion of the boundary layer, while the 2V1 motions are dominant in the outer region of the boundary layer. The cross-over point for the two patterns is seen to be at approximately $0.5\delta$. Thus, the back edge of the structures is followed by downward motions for $y/\delta < 0.5$ and by upward motions for $y/\delta > 0.5$. Since the large-scale structures are convecting at less than $0.9U_\infty$, and the fluid upstream of the structures has excess streamwise momentum, a saddle point is implied on the back of the organized structures in a reference frame coincident with them, as indicated earlier in §5.2. Care must be taken when drawing conclusions about instantaneous streamlines in a turbulent flow field, since the character of the fluctuating velocity field depends directly upon the magnitude of the mean velocity (see, for example, Lim 1979). To deduce a true saddle point in terms of the instantaneous streamlines, the convection velocity of the structure must be nearly equal to the local mean velocity; this is approximately true at $y/\delta = 0.5$, where $U/U_\infty \approx 0.92$.

The analysis in this section has shown that the ensemble-averaged flow field presented earlier is representative of individual large-scale motions which occur in this supersonic boundary layer. However, it should not be assumed that the identification of this particular type of individual structure precludes the existence of other types of large-scale structures.

### 5.4. *The relation between +VITA events and the Reynolds shear stress*

The correspondence between the upstream interface of large-scale motions and significant shear product contributions has been illustrated above. To quantify this relationship, the contribution to the long-time-averaged shear stress can be calculated near the individual VITA events. A window was chosen to correspond to

the length of the +VITA event, $T^* = \pm 0.6$. The values of $(\rho u)'v'$ in the window about every event were summed and then divided by the total number of points in the record, not just the number of points in the events. Throughout most of the boundary layer, the +VITA contribution ($k_V = 1.0$) is approximately equal to 40% of the total Reynolds stress. The choice of window and threshold has an effect on the contribution, and by varying these parameters an entire range of values can be found. The important result is that, at physically reasonable choices of threshold and window size, the contributions to the long-time-averaged shear stress are significant. Furthermore, these contributions are made in a relatively small fraction of the total time. With the parameters used above, the windows comprise a maximum of 25% of the total record.

Since 40% of the Reynolds stress occurs near +VITA events, a significant portion of the shear stress comes from motions not associated with large-scale +VITA events. This indicates that, while the large-scale motions detected by +VITA are significant in the outer layer, there are certainly other shear-stress producing motions in the boundary layer.

While this analysis establishes a link between the large-scale motions and Reynolds stress production, it does not necessarily imply that the bulges themselves create the shear stress. Another possible interpretation is that smaller-scale, Reynolds-stress-producing motions are located along the upstream edge of the large-scale bulge. The notion that these motions are of smaller scale is consistent with the higher frequency content of the $(\rho u)'v'$ spectrum (Fernando *et al.* 1987*a*). This interpretation also represents an extension of Falco's (1977) 'typical eddy' argument to very high Reynolds number. In, fact, recent Rayleigh scattering visualization of a supersonic boundary layer indicates that small-scale motions are associated with the upstream edge of the large-scale bulges (Smith 1989). As pointed out by Smits *et al.* (1989), however, Falco's typical eddies are much too small to be discerned with the instrumentation used here, and the effects ascribed by him to small-scale motions would then be ascribed here to much larger-scale motions. It should be noted that the Rayleigh scattering visualization shows smaller-scale motions located elsewhere in the boundary layer as well. This, in turn, is consistent with the result that not all of the shear stress occurs near the upstream edge of the large-scale structures.

## 6. Summary and final discussion

### 6.1. *Summary of results and conclusions*

This paper has presented the results of an experimental investigation into the large-scale physical structure of a zero-pressure-gradient turbulent boundary layer in supersonic flow. Previous studies have indicated that a hierarchy of structure heights populate the boundary layer, with the largest structures extending across the entire boundary layer. In the present work, many details of these large-scale motions have been investigated. It was seen that the correlation between two vertically-spaced hot wires persists over a distance greater than $0.6\delta$. The average inclination angle of the organized structures is 45–60° across most of the boundary layer, with a decrease near the wall, and an increase towards the edge of the boundary layer. The standard deviation of the individual structure angles about this average is approximately 20° throughout the boundary layer, as shown by Spina & Smits (1987).

The average spanwise extent of the organized structures is slightly less than the vertical extent, but is still comparable to the boundary-layer thickness. The broad-band correlation between two hot wires suggests an average spanwise extent of

$0.4$–$0.5\delta$, although the width of the structures which contribute to the cross-correlation increases with $y/\delta$.

Broadband analysis of two hot wires separated by less than $0.2\delta$ in the streamwise direction reveals a convection velocity of $0.9U_\infty$, consistent with a method in which only the contribution from large-scale structures is considered. The convection velocity was found to be nearly uniform in the outer region of the boundary layer ($y/\delta > 0.2$).

A sharp streamwise mass-flux gradient is coincident with the upstream interface of the large-scale structures (the back of the structures). The steep gradient occurs at the interface where the high-momentum fluid upstream of the structure meets the low-momentum fluid within the structure. This interface is detected by the VITA conditional sampling technique (positive events). Because the sharp gradient is the dominant feature in the streamwise mass-flux signal, it is the primary contributor to the broad-band correlations. This is supported by the correspondence between typical correlation lengthscales and structure angles and those determined through conditional sampling. Flow visualization evidence by Smith & Smits (1988) also indicates a correspondence between the large-scale structures and a sharp streamwise mass-flux gradient.

There appears to be a direct relationship between the sharp streamwise gradient at the upstream edge of the structure and strong shear stress motions surrounding the 'back'. The most frequently occurring motion downstream of the steep gradient is a quadrant 2 motion (low momentum, positive normal velocity), although quadrant 3 motions do occur. Upstream of the gradient, quadrant 4 motions (high momentum, negative normal velocity) are predominant in the lower half of the boundary layer, while quadrant 1 motions (high momentum, positive normal velocity) are the primary motions in the upper half of the boundary layer. This structural flow field suggests that there is a stagnation point on the back of a significant fraction of the organized structures at approximately $0.5$–$0.7\delta$, in a reference frame moving with the large-scale structures. This large-scale motion accounts for about 40% of the Reynolds shear stress throughout the boundary layer. The intermittent nature of the boundary layer is revealed by the fact that this 40% contribution occurs in less than 25% of the total time. These characteristics are consistent with similar observations in low-speed incompressible flows.

The detected large-scale structures do not produce significant amounts of turbulent energy, nor do they have any direct connection to the near-wall structure (the high Reynolds number of the boundary layer ensures that the scales of the near-wall and delta-scale motions are orders of magnitude apart). Yet, the importance of the large-scale turbulent bulge can be seen in the following:

(i) The passage of the large-scale bulges affect the wall layer, as evidenced by the correlation between wall-pressure peaks and positive VITA events detected in the outer region (Spina & Smits 1987). Also, Robinson (1986*a*) was able to correlate the mass flux signals from a hot wire at $y^+ = 29$ with one in the outer region of a supersonic boundary layer.

(ii) Significant levels of Reynolds stress are associated with the large-scale structures. As noted previously, the Reynolds stress may be produced by the bulge itself, or it may be created by smaller-scale motions associated with the upstream interface of the bulge.

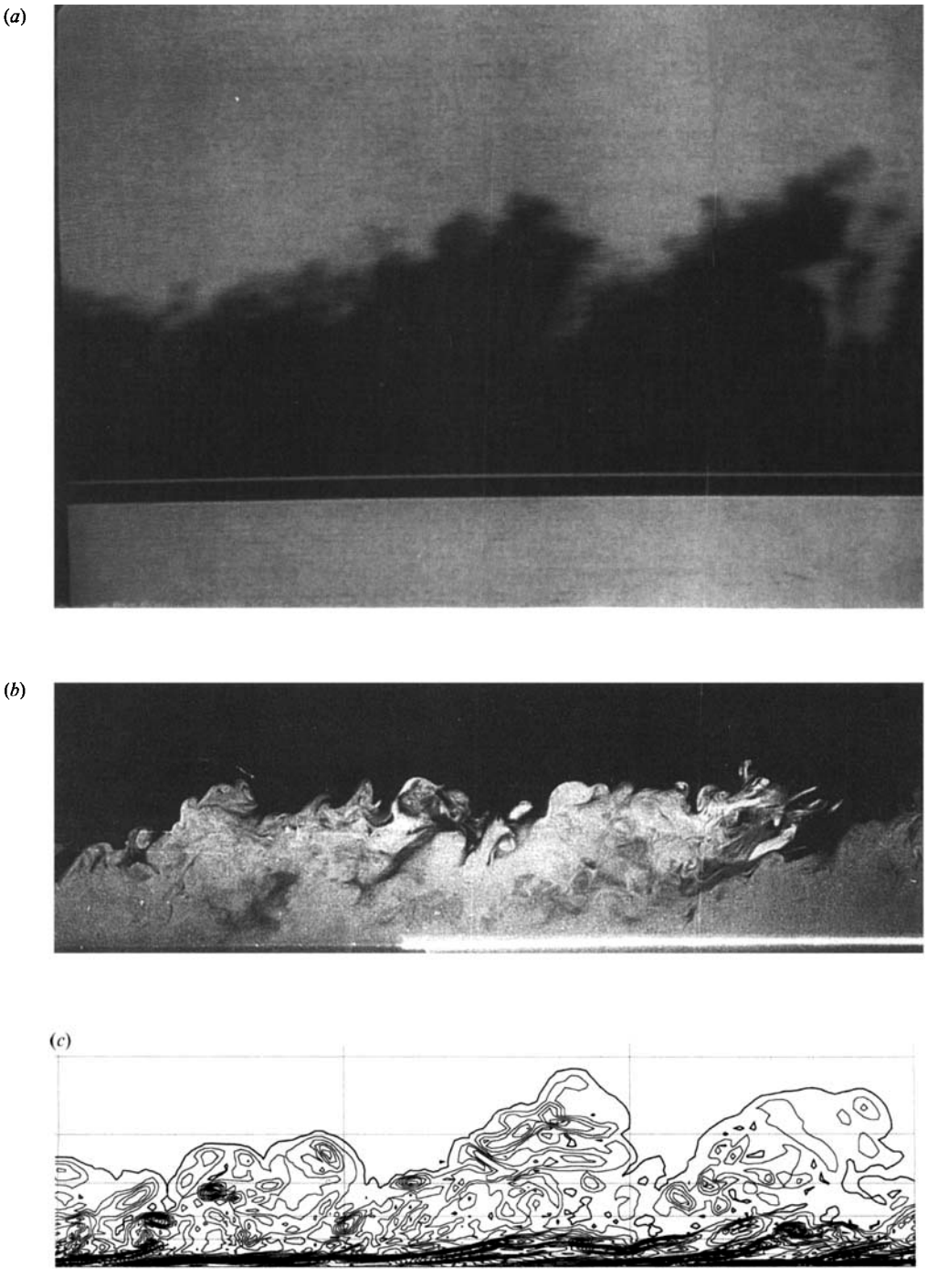


FIGURE 20. (a) Streamwise cross-section of a supersonic boundary layer with $Re_\theta = 25000$, obtained using Rayleigh scattering; Smith (1989). (b) Streamwise cross-section of a subsonic boundary layer with $Re_\theta = 4000$, obtained using oil droplet visualization; Falco (1977). (c) Streamwise cross-section of a computer-generated subsonic boundary layer with $Re_\theta = 670$, showing iso-vorticity contours. The flow is a direct Navier–Stokes turbulence simulation; Robinson (1989).

### 6.2. *Mach-number versus Reynolds-number effects*

It remains to comment on the differences between the large-scale structure of low-speed and high-speed boundary layers, and on the role the Mach and Reynolds numbers play in the dynamics of this supersonic boundary layer.

Streamwise cross-sections of three boundary layers with greatly disparate Reynolds numbers are given in figure 20. Flow visualization of a Mach 2.5 boundary layer with $Re_\theta = 25000$ is shown in figure 20(*a*). The cross-section was obtained using Rayleigh scattering, and it shows (at least approximately) the instantaneous density field (Smith 1989). Figure 20(*b*) is a cross-section of a low-speed boundary layer with $Re_\theta = 4000$. The image was obtained using a vertical light-sheet to illuminate a fog of oil droplets (Falco 1977). While the boundary layers visualized in figure 20(*a*) and 20(*b*) are naturally occurring, the flow illustrated in figure 20(*c*) was generated from a direct Navier–Stokes turbulence simulation and has $Re_\theta = 670$ (Robinson 1990). In this case, the streamwise cross-section shows iso-vorticity contours. Each of these figures clearly shows the large-scale bulges which have been described by researchers in subsonic flow (Brown & Thomas 1977; Blackwelder & Kovasznay 1972; Falco 1977, etc.) and have now been identified in supersonic flow.

At first sight, there does not appear to be a significant Reynolds-number effect on the characteristics of the large-scale structures. The delta-scale bulges possess the same attributes at $Re_\theta \approx 10^5$ as at $Re_\theta \approx 10^3$, as evidenced by the quantitative results presented in this paper and by the qualitative visualization shown in figure 20. The insensitivity of the largest organized structures to Reynolds number is not surprising, however. Increasing Reynolds number merely serves to increase the number of scales in the boundary layer, thereby accentuating the size difference between the smallest and largest scale motions. In particular, as noted earlier, the smaller motions that appear on the back of the delta-scale motions (i.e. Falco's typical eddies) are approximately 200 viscous units in size for the low-Reynolds-number flows, and about 1000 viscous units in the high-Reynolds-number supersonic flow. Now, a change in Reynolds number does not necessarily imply a change in the role or dynamics of a certain motion; i.e. the underlying physics need not change, just the relationship between scales. Similarly, Reynolds number effects on the near-wall structures are probably small, although the effective Reynolds number near the wall is significantly less than the quoted $Re_\theta$ due to the increased dynamic viscosity there ($\nu_{\text{wall}} \approx 5\nu_\infty$).

Although we possess no experimental evidence in the near-wall region of supersonic boundary layers, there does not seem to be any reason to suppose that the near-wall structures are altered due to Reynolds number effects (e.g. the scaling of streak spacing and bursting will not change from that documented in low-speed flows). However, because of the increased size difference between the near-wall structures and the delta-scale motions (the influence of the near-wall motions is usually considered to extend to about 100 wall units, and in this boundary layer $\delta \approx 10000$ wall units), the degree of interaction of the organized structures may change appreciably with increasing Reynolds number. For example, it has been suggested that pairing of near-wall structures may be the method by which large-scale structures are created. At low Reynolds numbers (say $Re_\theta \approx 1000$) only about two to three pairings of the smallest-scale structures would lead to delta-scale structures. In contrast, at the Reynolds number considered here, nearly ten pairings would be required to transition from the smallest to the largest structures because of the large size difference in scales. Such a large number of pairings would seem to indicate that

this type of interaction is unlikely to occur in such a complex, time-dependent flow. Clearly, research must be performed in the near-wall region of high-speed boundary layers to explore the interaction of the different-scale motions.

Before discussing the effect of compressibility on the large-scale structure of turbulent boundary layers, a distinction should be made between fluid property variations in a compressible boundary layer and true compressibility effects (or Mach number effects). A compressible boundary layer, by its very nature, contains fluid property variations; most notably density stratification. However, significant fluid property variations can also be obtained in a highly-heated, incompressible boundary layer (e.g. Cheng & Ng 1982).

Fluid property variations can be expected to lead to some differences between either compressible or heated, incompressible boundary layers and unheated, incompressible boundary layers, since the vorticity transport equation describes the transport of vorticity per unit mass. Therefore, both mean and instantaneous density gradients will affect the vorticity dynamics in the boundary layer. Also, Brown & Roshko (1974) found that density variations can significantly affect the growth rate of a subsonic mixing layer. It may follow that fluid property variations affect the scales of motions in general. This could explain some of the scale differences between this compressible boundary layer and the unheated, incompressible layer studied by Alving (1988) (if it is argued that the scales of the structures are determined by the conditions near the wall, where fluid property variations are greatest).

On the other hand, true compressibility effects occur when the relative Mach number between interacting fluid elements is significant (roughly greater than 0.5). One of the distinguishing characteristics of the large-scale structure documented in this flow is the upstream interface, where high-momentum fluid interacts with the low-momentum structure. Since the three-dimensional bulge convects at $0.9U_\infty$, the entrained fluid flows over the top and around the sides of the 'retarded' structure. If there are compressibility effects on the large-scale structure, they would manifest themselves at this interface, where the relative Mach number is greatest. However, the relative Mach number for this turbulent bulge is $0.1 \times M_\infty \approx 0.3$, which is too low to introduce significant compressibility effects. Clearly, however, relative Mach number effects will become more important as the free-stream Mach number increases towards hypersonic values. In this particular boundary layer, Mach-number effects are probably only important for moderate-scale structures lower in the boundary layer which convect at slower speeds (the 'moderate-scale' structures observed convecting at $0.6U_\infty$ in a transitional Mach 3.5 boundary layer by Jedlicka, Wilkins & Seiff (1954) were turbulent spots). Thus, while compressibility affects this turbulent boundary layer in general through fluid property variations, it appears that compressibility, as such, does not affect the delta-scale bulges.

This work was supported by the Air Force Office of Scientific Research through Grant 88-0120, monitored by Dr James McMichael.

## Appendix A

An important difference exists between the use of hot wires in compressible and incompressible flows: normal and crossed hot wires yield density-weighted quantities in supersonic flow. The hot wires respond to the fluctuating streamwise mass flux, $(\rho u)'$, and not simply the fluctuating streamwise velocity, $u'$, although the crossed

wire does yield a signal proportional to the normal velocity, $v'$. Without separate data on the instantaneous temperature, estimates of $u'$ and $\overline{(u'^2)}^{\frac{1}{2}}$ can be obtained from $(\rho u)'$ and $\overline{((\rho u)'^2)}^{\frac{1}{2}}$, respectively, with the aid of the strong Reynolds analogy (SRA) (Morkovin 1962). For an adiabatic wall in a zero-pressure-gradient flow, Morkovin showed that the main assumption of the SRA, $T_0' = 0$, leads to

$$\frac{T'}{\bar{T}} = -(\gamma-1)M^2\frac{u'}{\bar{u}}.$$

This is akin to the assumption that the correlation between the fluctuating velocity and the fluctuating static temperature, $R_{Tu}$, is $-1.0$. If $p'/\bar{p} \ll \rho'/\bar{\rho}$, it follows that

$$\frac{\rho'}{\bar{\rho}} = (\gamma-1)M^2\frac{u'}{\bar{u}}. \tag{A 1}$$

This expression allows $u'$ to be derived from the measured $(\rho u)'$ by performing a Reynolds decomposition:

$$(\rho u)' = (\rho u) - \overline{(\rho u)},$$
$$(\rho u)' = \rho'\bar{u} + \bar{\rho}u' + \rho'u' - \overline{\rho'u'}.$$

Neglecting the second-order terms, it becomes evident that mass-flux fluctuations have contributions from two sources, velocity fluctuations and density fluctuations:

$$(\rho u)' = \rho'\bar{u} + \bar{\rho}u'. \tag{A 2}$$

Applying the SRA result (equation (A 1)) to (A 2),

$$\frac{(\rho u)'}{\bar{\rho}\bar{u}} = [1+(\gamma-1)M^2]\frac{u'}{\bar{u}}, \tag{A 3}$$

where the $(\gamma-1)M^2$ term indicates the contribution of the density fluctuations, $\rho'/\bar{\rho}$, to the mass-flux fluctuations.

As shown by Morkovin (1962), Kistler (1959), and by Gaviglio (1987), the assumption of negligible stagnation temperature fluctuations is not well-supported by experiment. Dussauge & Gaviglio (1981) measured $R_{Tu}$ to be $-0.8$, in contrast to the value specified by the SRA, $-1.0$. The one-dimensional small-perturbation energy equation and the SRA result $\overline{T'^2}/\bar{T}^2 = [(\gamma-1)M^2]^2\overline{u'^2}/\bar{u}^2$ can be used to derive the relation $T'_{0_{\rm rms}} = T'_{\rm rms}(2(1+R_{Tu}))^{\frac{1}{2}}$, implying that the stagnation temperature fluctuations are approximately 60% of the static temperature fluctuations at Mach numbers where the pressure fluctuations are not large. While not exact because of the use of the SRA, this result nonetheless shows that stagnation temperature fluctuations may indeed be significant.

Because of the questionable application of the strong Reynolds analogy in determining the instantaneous quantities, the use of (A 3) was avoided wherever possible in this paper, and the instantaneous results are given in terms of $(\rho u)'$. While a strict use of the SRA to deduce instantaneous quantities does not seem to be warranted, the mass-flux fluctuations can still be considered proportional to streamwise velocity fluctuations, at least approximately. Note that the ratio of $u'$ to $(\rho u)'$ varies across the boundary layer since the relative contribution of the density fluctuations to the mass-flux fluctuations depends on the square of the Mach number (equation (A 3)). In this paper, $(\rho u)'$ is normalized by the local value of $(\rho u)'_{\rm rms}$ to minimize the influence of this variation.

The strong Reynolds analogy is also used to determine $u'_{\rm rms}$. An expression for $(\overline{u'^2})^{\frac{1}{2}}$ in terms of the measured $(\overline{(\rho u)'^2})^{\frac{1}{2}}$ can be derived from (A 3):

$$\frac{(\overline{(\rho u)'^2})^{\frac{1}{2}}}{\bar{\rho}\bar{u}} = [1+2(\gamma-1)M^2+((\gamma-1)M^2)^2]^{\frac{1}{2}}\frac{(\overline{u'^2})^{\frac{1}{2}}}{\bar{u}}. \tag{A 4}$$

However, if a 'milder' application of the strong Reynolds analogy,

$$\frac{(\overline{\rho'^2})^{\frac{1}{2}}}{\bar{\rho}} = (\gamma-1)M^2\frac{(\overline{u'^2})^{\frac{1}{2}}}{\bar{u}}, \tag{A 5}$$

is used in conjunction with the root-mean-square of (A 2), the following relation between $u'_{\rm rms}$ and $(\rho u)'_{\rm rms}$ results:

$$\frac{(\overline{(\rho u)'^2})^{\frac{1}{2}}}{\bar{\rho}\bar{u}} = [1+2R_{\rho u}(\gamma-1)M^2+((\gamma-1)M^2)^2]^{\frac{1}{2}}\frac{(\overline{u'^2})^{\frac{1}{2}}}{\bar{u}}. \tag{A 6}$$

Here the experimentally-based value for $R_{Tu}$ $(=-0.8\approx -R_{\rho u})$ can be used instead of the value of $-1.0$ assumed in the stronger application of the SRA. Note that the key to this more accurate result is a slightly weaker application of the SRA; i.e. the relation between $\rho'$ and $u'$ is assumed to hold in a time-averaged sense rather than instantaneously (see also Gaviglio 1987).

Some recent papers have made a distinction between (A 1) and (A 5) by denoting them as the *strong Reynolds analogy* and the *very strong Reynolds analogy*, respectively. Strictly speaking, however, both result from the application of the strong Reynolds analogy since both require $T'_0 = 0$. However, it has been shown that (A 1) is not strictly valid, whereas (A 5) has been experimentally verified (Dussauge & Gaviglio 1981).

## Appendix B

A brief discussion of the turbulent inertia terms which result when the compressible $x$-momentum equation is Reynolds averaged will aid in the interpretation of the crossed-wire data. The compressible Reynolds-averaged equation is more complex than the corresponding incompressible one. In addition to the two mean convective terms, the following terms are potentially significant in a boundary layer:

$$\frac{\partial}{\partial y}(\bar{\rho}\overline{u'v'}+\bar{u}\overline{\rho'v'}+\bar{v}\overline{\rho'u'}+\overline{\rho'u'v'}).$$

These terms are similar in nature to the single fluctuating product term which results from the same analysis in incompressible flow, and can therefore be classified as 'apparent' or turbulent stresses. The third term can be neglected because $\bar{v} \ll \bar{u}$ in a boundary layer, and the fourth term is of second order compared to the remaining terms. The turbulent stress in a compressible boundary layer is therefore approximated by

$$\tau_{\rm turb} = -\bar{\rho}\overline{u'v'}-\overline{\rho'v'}\bar{u},$$

where the first term is the 'traditional' Reynolds stress as in the incompressible case, and the second term is an apparent stress due to density fluctuations. By a direct extension of the analysis presented in Appendix A, it can be shown that the quantity measured by the crossed wire, $(\rho u)'v'$, contains both of these shear stresses:

$$(\rho u)'v' = \bar{u}\rho'v'+\bar{\rho}u'v'.$$

Because of the two different contributions to the compressible turbulent stress, care must be taken when discussing the 'Reynolds stress' in a compressible flow. Although the contribution due to density fluctuations is a real one, it is usually separated out when making a direct comparison between compressible and incompressible Reynolds stress. A relation which eliminates the shear stress contribution due to density fluctuations can be found by extending (A 3)

$$\frac{(\rho u)'v'}{\bar{\rho}\bar{u}^2} = [1+(\gamma-1)M^2]\frac{u'v'}{\bar{u}^2},$$

(note that this result depends upon the stronger of the two strong Reynolds analogy results, the instantaneous form). Owing to the uncertainty associated with the use of the SRA, the 'density-weighted' shear stress, $\overline{(\rho u)'v'}$, and the density-weighted shear product, $(\rho u)'v'$, were used exclusively in this paper. As in the interpretation of $(\rho u)'$, the contribution of the density fluctuations to $(\rho u)'v'$ varies with distance from the wall since $M = M(y)$. This makes definitive statements concerning the equivalence of $\overline{(\rho u)'v'}$ and the Reynolds stress difficult, and only an approximate proportionality can be claimed between the two quantities.

## REFERENCES


Acarlar, M. S. & Smith, C. R. 1987 A study of hairpin vortices in a laminar boundary layer. Part 1. Hairpin vortices generated by a hemisphere protuberance. *J. Fluid Mech.* **175**, 1.

Alving, A. E. 1988 Boundary layer relaxation from convex curvature. PhD thesis, Dept. of Mechanical & Aerospace Engineering, Princeton University, Princeton, NJ.

Alving, A. E. & Smits, A. J. 1988 Correlation measurements and structure angles in a turbulent boundary layer recovering from convex curvature. *Zarić Memorial International Seminar on Near-Wall Turbulence, Dubrovnik, Yugoslavia, p.* 507.

Black, T. J. 1968 An analytical study of the measured wall pressure field under supersonic turbulent boundary layers. *NASA* CR-888.

Blackwelder, R. & Kaplan, R. E. 1976 On the wall structure of the turbulent boundary layer. *J. Fluid Mech.* **76**, 89.

Blackwelder, R. F. & Kovasznay, L. S. G. 1972 Time scales and correlations in a turbulent boundary layer. *Phys. Fluids* **15**, 1545.

Brown, G. L. & Roshko, A. 1974 On density effects and large structure in turbulent mixing layers. *J. Fluid Mech.* **64**, 775.

Brown, G. L. & Thomas, A. S. W. 1977 Large-scale structure in a turbulent boundary layer. *Phys. Fluids* **20**, 243.

Chen, C. P. & Blackwelder, R. F. 1978 Large-scale motion in a turbulent boundary layer: a study using temperature contamination. *J. Fluid Mech.* **89**, 1.

Cheng, R. K. & Ng, T. T. 1982 Some aspects of strongly heated turbulent boundary layer flow. *Phys. Fluids* **25**, 1333.

Deckker, B. E. L. & Weekes, M. E. 1976 The unsteady boundary layer in a shock tube. *Inst. Proc. Mech. Engng* **190**, 287.

Deckker, B. E. L. 1980 An investigation of some unsteady boundary layers by the schlieren method. *Intl Symp. on Flow Visualization, Ruhr Universitat.*

Donovan, J. F. 1989 The structure of supersonic turbulent boundary layers subjected to concave surface curvature. PhD thesis, Dept. of Mechanical & Aerospace Engineering, Princeton University, Princeton, NJ.

Donovan, J. F. & Spina, E. F. 1990 An improved analysis of crossed-wire signals obtained in supersonic flow. *Symp. on the Heuristics of Thermal Anemometry*, p. 41. Spring 1990 Meeting of the ASME Fluids Engineering Division, Toronto, Canada.

Dussauge, J.-P. & Gaviglio, J. 1981 Bulk dilatation effects on Reynolds stress in the rapid

expansion of a turbulent boundary layer at supersonic speed. *Proc. Third Symp. on Turbulent Shear Flows, University of California, Davis*, p. 2.33.

FALCO, R. E. 1977 Coherent motions in the outer region of turbulent boundary layers. *Phys. Fluids* **20**, S124.

FERNANDO, E. M., DONOVAN, J. F. & SMITS, A. J. 1987*a* The calibration and operation of a constant-temperature crossed-wire probe in supersonic flow. *Symp. on Thermal Anemometry, Columbus, Ohio*, p. 43. ASME.

FERNANDO, E. M., SPINA, E. F., DONOVAN, J. F. & SMITS, A. J. 1987*b* Detection of large-scale organized motions in a turbulent boundary layer. *Sixth Symp. on Turbulent Shear Flows, Toulouse, France*, p. 16-8-1.

GAVIGLIO, J. 1987 Reynolds analogies and experimental study of heat transfer in the supersonic boundary layer. *Intl J. Heat Mass Transfer* **30**, 911.

HEAD, M. R. & BANDYOPADHYAY, P. 1981 New aspects of turbulent boundary layer structure. *J. Fluid Mech.* **155**, 441.

JAMES, C. S. 1958 Observations of turbulent-burst geometry and growth in supersonic flow. *NASA* TN4235.

JEDLICKA, J. R., WILKINS, M. M. & SEIFF, A. 1954 Experimental determination of boundary layer transition on a body of revolution at $M = 3.5$. *NACA* TN3342.

KISTLER, A. L. 1959 Fluctuation measurements in a supersonic turbulent boundary layer. *Phys. Fluids* **2**, 290.

KOVASZNAY, L. S. G., KIBENS, V. & BLACKWELDER, R. F. 1970 Large-scale motion in the intermittent region of a turbulent boundary layer. *J. Fluid Mech.* **41**, 283.

LIM, T. T. 1979 Coherent structure in coflowing jets and wakes. PhD thesis, Department of Mechanical Engineering, University of Melbourne, Melbourne, Australia.

MORKOVIN, M. V. 1962 Effects of compressibility on turbulent flows. *Intl Symp. on the Mechanics of Turbulence, CNRS, Paris, France.*

OFFEN, G. R. & KLINE, S. J. 1975 A proposed model of the bursting process in turbulent boundary layers. *J. Fluid Mech.* **70**, 209.

OWEN, F. K. & HORSTMAN, C. C. 1972 On the structure of hypersonic turbulent boundary layers. *J. Fluid Mech.* **53**, 611.

PRATURI, A. K. & BRODKEY, R. S. 1978 A stereoscopic visual study of coherent structures in turbulent shear flow. *J. Fluid Mech.* **89**, 251.

RAJAGOPALAN, S. & ANTONIA, R. A. 1979 Some properties of the large-scale structure in a fully developed turbulent duct flow. *Phys. Fluids* **22**, 614.

ROBINSON, S. K. 1986*a* Space–time correlation measurements in a compressible turbulent boundary layer. *AIAA Paper* 86-1130.

ROBINSON, S. K. 1986*b* Instantaneous velocity profile measurements in a turbulent boundary layer. *Chem. Engng Commun.* **43**, 347.

ROBINSON, S. K. 1989 A review of vortex structures and associated coherent motions in turbulent boundary layers. *Proc. Second IUTAM Symp. on Structure of Turbulence and Drag Reduction, Zurich, Switzerland.*

ROBINSON, S. K. 1990 Kinematics of turbulent boundary layer structure. PhD thesis, Mechanical Engineering Department, Stanford University, Stanford, CA.

ROBINSON, S. K., KLINE, S. J. & SPALART, P. R. 1988 Quasi-coherent structures in the turbulent boundary layer: Part II. Verification and new information from a numerically-simulated flat-plate layer. *Zarić Memorial International Seminar on Near-Wall Turbulence, Dubrovnik, Yugoslavia*, p. 218.

SEIFF, A. & SHORT, B. J. 1958 An investigation of supersonic turbulent boundary layers on slender bodies of revolution in freeflight by use of a Mach-Zehnder interferometer and shadowgraph. *NASA* TN4364.

SMITH, C. R. 1984 A synthesized model of the near-wall behavior in turbulent boundary layers. *Proc. of the Eighth Symp. on Turbulence, University of Missouri–Rolla* (ed. G. K. Patterson & J. L. Zakin).

SMITH, M. W. 1989 Flow visualization in supersonic turbulent boundary layers. PhD thesis, Dept. of Mechanical & Aerospace Engineering, Princeton University, Princeton, NJ.

SMITH, M. W. & SMITS, A. J. 1988 Cinematic visualization of coherent density structures in a supersonic turbulent boundary layer. *AIAA Paper* 88-0500.

SMITS, A. J. & DUSSAUGE, J.-P. 1989 Hot-wire anemometry in supersonic flow. *AGARDograph* 315 (ed. H. H. Fernholz, P. J. Finley, J.-P. Dussauge & A. J. Smits).

SMITS, A. J., HAYAKAWA, K. & MUCK, K. C. 1983 Constant-temperature hot-wire anemometry practice in supersonic flows. Part 1. The normal wire. *Exps Fluids* **1**, 83.

SMITS, A. J., SPINA, E. F., ALVING, A. E., SMITH, R. W., FERNANDO, E. M. & DONOVAN, J. F. 1989 A comparison of the turbulence structure of subsonic and supersonic boundary layers. *Phys. Fluids* A **1**, 1865.

SPINA, E. F. 1988 Organized structures in a supersonic turbulent boundary layer. PhD thesis, Dept. of Mechanical & Aerospace Engineering, Princeton University, Princeton, NJ.

SPINA, E. F. & SMITS, A. J. 1987 Organized structures in a compressible, turbulent boundary layer. *J. Fluid Mech.* **182**, 85.

THEODORSEN, T. 1952 Mechanism of turbulence. In *Proc. Second Midwestern Conf. on Fluid Mechanics, Ohio State University.*

TRAN, T. T. 1987 An experimental investigation of unsteadiness in swept shock wave/turbulent boundary layer interactions. PhD thesis, Princeton University, Princeton, NJ.

WALLACE, J. M., ECKELMANN, H. & BRODKEY, R. S. 1972 The wall region in turbulent shear flow. *J. Fluid Mech.* **54**, 39.

WILLMARTH, W. W. & LU, S. S. 1972 Structure of the Reynolds stress near the wall. *J. Fluid Mech.* **55**, 65.

WILLMARTH, W. W. & TU, B. J. 1967 Structure of turbulence in the boundary layer near the wall. *Phys. Fluids* **10**, S134.

ZAKKAY, V., BARRA, V. & WANG, C. R. 1979 The nature of boundary-layer turbulence at a high subsonic speed. *AIAA J.* **17**, 356.